SUPPLEMENTARY INFORMATION

Complete Reductive Defluorination of PFAS in Water Under Ambient Conditions via Plasmon-Enhanced Catalysis

Authors: Ozce Durak[a, §], Seung Soo S. Lee[a, §], Lydia Watt[a], Susanna Maisto[a], Fabian Menges[b], Changwoo Kim[c], James M. Mayer[b], and John D. Fortner[a, *]

[a] Department of Chemical and Environmental Engineering, Yale University, New Haven, CT, 06511 United States

[b] Department of Chemistry, Yale University, New Haven, CT, 06517 United States

[c] Department of Environment and Energy Engineering, Gwangju Institute of Science and Technology, Gwangju, 61005, Republic of Korea

§These authors contributed equally to this work.

*To whom correspondence should be addressed:

John D. Fortner: Tel: +1-314-935-9293; Email: john.fortner@yale.edu

Keywords: PFAS destruction, reductive defluorination, water treatment, PFOA, PFOS, plasmonic photocatalysis, LSPR

Experimental Section

Materials

Cetyltrimethylammonium bromide (CTAB, >99.0%), tetraethyl orthosilicate (TEOS, 98%) triethanolamine (TEA, >99.0%), (aminopropyl)triethoxysilane (APTES, 99%), chloroplatinic acid hydrate ($H_2PtCl_4 \cdot xH_2O$, >99.9%), sodium tetrachloropalladate (Na_2PdCl_4, 99.99%), trisodium citrate dihydrate (US Pharmacopeia grade), sodium borohydride ($NaBH_4$, 99%), silver nitrate ($AgNO_3$, >99.0%), perfluorooctanoic acid (PFOA, >95.0%), superoxide dismutase (SOD, >95.0%), ethylenediaminetetraacetic acid (EDTA, >99.0%), tert-butanol (TBA, anhydrous, ≥99.5%), isopropanol (IPA, ≥99.5%), methanol (MeOH, 99.95%), and ethanol (EtOH, 200 proof, anhydrous, 99.5%) were purchased from Sigma Aldrich. Perfluorooctanesulfonic acid (PFOS, >99.0%) was purchased from TCI. All experiments were conducted in ultra-pure Milli-Q water (MQ water, 18.2 MΩ·cm) using quartz reactors.

Synthesis

Mesoporous Silica Nanoparticle Supports (MSN). CTAB (5.72 g, 15.69 mmol) was dissolved in ethanol (18 g, 0.39 mol) and water (129.6 g, 7.2 mol) under stirring (750 rpm) at room temperature (RT) for 30 min. In the CTAB micelle-containing solution, TEA (0.568 g, 3.81 mmol) was added at RT and agitated for an additional 30 min. The final pH was recorded as approximately 9.0±0.5 at RT. The mixture was then heated to 70 °C (ramp rate of 10 °C/min) under vigorous agitation (at 750 rpm). Then, TEOS (66.28 mmol) was injected into the solution at the injection rate of 1000 μL/min, and the whole mixture was continuously stirred at 750 rpm and 70 °C for 2 h under N_2 flow. The resulting cloudy solution was further purified using HCl-containing ethanol (1.0 wt.% HCl in ethanol) and separated by centrifugation (at 13,751 rcf for 25 min). The purified MSN was dried and kept under vacuum overnight. The as-synthesized MSN was further purified under acidic conditions at a high temperature above 70 °C to remove CTAB and TEA within the MSN pore space. 4000 mg of MSN was homogenously dispersed in HCl-containing ethanol (120 mL) at pH below 1.0 (typically 2 wt.% HCl in ethanol) and agitated at 70 °C for 3 h. The purified MSN was cooled and separated by centrifugation (13,750 rcf for 40 min). The CTAB removal process was repeated 3 times[1]. As synthesized, MSN exhibits a significantly larger surface area compared to nanoscale silica prepared by the Stöber method, a conventional approach, which has a BET surface area of 34.9 m^2/g for particle sizes of approximately 200 nm, as reported elsewhere[2].

MSN Amine surface modification (MSN-NH_2). Primary amine functionalization on MSN was achieved via post-synthesis surface modification with APTES. Before the reaction, MSN samples were purified under acidic conditions to remove CTAB and TEA as described above. APTES (6 mL, 25.64 mmol) was added to the purified MSN (1000 mg) containing ethanol/water (120 mL/60 mL) co-solvent at RT under vigorous agitation (at 750 rpm) and heated to 70 ^oC (ramp rate of 10 ^oC/min). The reaction mixture was stirred at 70 ^oC for 2 h under N_2 flow. The resulting cloudy solution was purified using ethanol and separated by centrifugation (at 13,750 rcf for 25 min) and stored in an amber bottle.

Palladium nanoparticles on MSN (MSN-NH_2-Pd). Palladium nanoparticles were nucleated and grown on primary amine functionalized MSN (MSN-NH_2) in aqueous media at 83 ^oC. All synthetic conditions were processed using palladium and citrate stock solutions; the palladium stock solution was 0.59 mol/L, and the citrate stock solution was 0.105 mol/L (in water). The stock solutions were prepared 1 day before the reaction and stored in the refrigerator (3-5 ^oC). Typically, to synthesize 5 wt.% Pd-loaded MSN-NH_2-Pd, 400 mg of MSN-NH_2 was dispersed in DI water (100 mL) at RT and stirred at 750 rpm under N_2 flow for 30 min. Homogeneously mixed MSN-NH_2 solution was then agitated with palladium stock solution (0.377 mL, 19.30 mg of Pd, 0.181 mmol) and sodium citrate stock solution (8.8 mL, 0.924 mmol) at RT. The temperature of the reaction was then heated to 83 ^oC (ramp rate of 10 ^oC/min) and kept at that temperature for a desired time (25, 60, and 120 min) under N_2 flow. After the reaction occurred at 83 ^oC, the reaction vessel was cooled immediately in an ice bath to stop growing Pd nanoparticles. The resulting brown precipitates (or gray/black, depending on Pd nanoparticle size and/or concentration) were purified using ethanol and water mixture, then separated by centrifugation at 13,750 rcf for 25 min. The purified MSN-NH_2-Pd particles were vacuum-dried overnight and kept in an amber vial.

Platinum nanoparticles on MSN (MSN-NH_2-Pt). Platinum nanoparticles were nucleated and grown on MSN-NH_2 in aqueous media at 90 ^oC. All synthetic conditions were processed using platinum and citrate stock solutions; the platinum stock solution was 0.50 mol/L, and the citrate stock solution was 0.105 mol/L (in water). The stock solutions were made 1 day before the reaction and stored in the refrigerator (3-5 ^oC). Typically, to make 3.7 wt.% Pt loaded MSN-Pt, 400 mg of MSN-NH_2 was dispersed in DI water (100 mL) at RT and stirred at 750 rpm under N_2 flow for 30 min. Homogeneously mixed MSN-NH_2 solution was then agitated with platinum stock solution

(0.715 mL, 31.00 mg of Pt, 0.159 mmol) and sodium citrate stock solution (6.6 mL, 0.693 mmol) at RT. The reaction temperature of the reaction was then heated to 95 ºC (ramp rate of 10 ºC/min) and kept at that temperature for a desired time (25, 60, and 120 min) under N_2 flow. After the reaction at 90 ºC, the reaction vessel was cooled immediately in an ice bath to stop the growth of Pt nanoparticles. The resulting yellow precipitates (or gray/black, depending on Pt nanoparticle size and/or concentration) were purified using ethanol and water, then separated by centrifugation at 13,750 rcf for 25 min. The purified MSN-NH_2-Pt was vacuum-dried overnight and kept in an amber vial.

Characterization

As-synthesized materials were characterized through established and standard methods including transmission electron microscopy (TEM), inductively coupled plasma-mass spectroscopy (ICP-MS), ultra-violet visible diffuse reflectance spectroscopy (UV-Vis DRS), and Brunauer-Emmett-Teller (BET) surface area analyzer. For details, the size and shape of the engineered nanomaterials was characterized through FEI Tecnai Osiris 200 KV TEM. TEM samples (10 mg of sample in 10 mL of ethanol) were bath-sonicated for several minutes, and a drop of the dispersed sample was subsequently placed onto a TEM grid and left to dry overnight at room temperature under ambient air. The elemental composition analysis of the nanomaterials was examined by ICP-MS (NexION 5000, Perkin Elmer) to determine the metal loading and NP integrity/dissolution (throughout 0 - 72 h experimental time frame) of the plasmonic photocatalysts. The analytical samples were digested in the boiling acid solution (typically 3:1 v/v ratio of HCl:HNO_3 at 100 ºC for 4 h). UV-vis DRS measurements of each sample were conducted by using Shimadzu UV-3600 Plus equipped with Fourier transform infrared spectrophotometer IRTracer-100. BET specific surface area of the engineered nanomaterials was analyzed using BET spectrometer (Micromeritics ASAP 2460 Surface Area and Porosity Analyzer) by N_2 adsorption isotherm at liquid nitrogen temperature (77 K). Before BET measurement, the sample was degassed at 110 ºC over 15 h under nitrogen flow using the sample degas system (Micrometritics FlowPrep 060).

Sorption experiments

Batch adsorption experiments were performed to assess the PFAS sorption performance of the plasmonic photocatalysts. 15 mL tubes were prepared with approximately 20 mg each particles (MSN-NH_2-Pd and MSN-NH_2-Pt) for the sorption experiment. 10 mL solutions of 1 to 500 ppm

PFAS were prepared, with 1000 ppm stock solutions and DI water bubbled with CO_2 to control pH, then added to each tube. Batch experiments were mixed on a rotating shaker for 24 h (in the dark) to achieve equilibrium; solution pH was measured at the start and end of the experiment. After each 24 h, 1.5 mL samples were taken and centrifuged. The supernatant was then sampled, diluted to achieve the relevant instrument concentration range, and analyzed with a Shimadzu Scientific Instruments 8060 Triple-Quad LC-MS system. Duplicate experiments were conducted, including blanks without plasmonic photocatalyst particles, for comparison and sorption capacity calculations at each equilibrium concentration. Equilibrium data (in aqueous and solid phases) were plotted, and Langmuir and Freundlich sorption models were assessed for each isotherm; for Freundlich isotherms, model fits were performed for the range below the maximum sorption capacity (approximated using the average of sorption capacity values at a maximum steady state). In addition to other isotherm parameters, maximum sorption capacity and half-saturation concentrations were calculated for each model fit. Corresponding equations for Langmuir (**Eq. 1**) and Freundlich (**Eq. 2**) isotherms are given below.

$$q_e = \frac{q_{max} b C_e}{1 + b C_e} \quad (1)$$

$$q_e = K_f {C_e}^n \quad (2)$$

Where q_e is the amount of contaminant adsorbed per gram of sorbent at equilibrium (mg/g), C_e is the equilibrium concentration of the contaminant in solution (mg/L or ppm), q_{max} is the maximum adsorption capacity (mg/g), and b is the Langmuir constant related to adsorption affinity (L/mg) in the Langmuir isotherm (**Eq. 1**); and K_f is the Freundlich constant indicative of adsorption capacity ((mg/g) $(L/mg)^{1/n}$), and n is the adsorption intensity (unitless) in the Freundlich isotherm (**Eq. 2**).

Photocatalytic reactions

Photocatalytic experiments were conducted under constant UV irradiation at 254 nm (UVC, Phillips, low-pressure mercury lamps, light intensity of 2.6 mW/cm^2) or 368 nm (UVA, USHIO, phosphor-coated low-pressure mercury lamps, light intensity of 7.3 mW/cm^2) in a 100 mL quartz vial. The reaction suspension consisted of 400 mg/L (ppm) of catalyst, 10 mg/L (ppm) of PFOA, and 2.5 mL of MeOH. Prior to UV irradiation, the quartz vial containing reaction suspension was sealed and bubbled with CO_2 (and H_2, if necessary) for 30 min. The working pH was maintained

in the range of 4.2-4.5 with the use of CO_2 bubbling before each experiment. Samples were collected at different reaction times (hourly for the first 4 h and then every 2 h until the 8th h) and analyzed accordingly for PFAS and F^- concentration. In the case of long-term experiments (up to 5 days) under constant UVA irradiation, sampling started at 24 h and was performed at 12 h intervals thereafter. The concentration of PFAS and corresponding byproducts were measured by using liquid chromatography coupled with mass spectroscopy (LC-MS, Shimadzu LCMS TQ 8060) while F^- concentration was determined by ion chromatography. The concentrations of PFOA and catalyst were kept constant in each scavenger experiment. Carbonate-bicarbonate buffer was used as the weak basic buffer in the pH study. For scavenger experiments, 2.5 mL TBA, 2.5 mL isopropanol, 400 mg $AgNO_3$, 100 mg SOD, and 100 mg EDTA were used. Reaction constants associated with stated scavengers can be given as; $k_{AgNO_3,\ e_{aq}^-} = 2.8 \times 10^9 M^{-1} \cdot s^{-1}$, $k_{AgNO_3,\ \mathrm{OH}} = 1.0 \times 10^{10} M^{-1} \cdot s^{-1}$ [3], $k_{SOD,\ O_2^{\bullet-}} = \sim 2 \times 10^9 M^{-1} \cdot s^{-1}$, $k_{\mathrm{SOD,\ OH}} = \sim 1.0 \times 10^{10} M^{-1} \cdot s^{-1}$) [4], $k_{EDTA,\ h^+} = 8.6 \times 10^9\ M^{-1} \cdot s^{-1}$ [5]. Photon flux, the number of photons incident per unit area per unit time, was calculated based on light intensity and wavelength to evaluate the availability of photons for catalytic processes. The resulting photon flux values were used to normalize reaction rates for direct comparison between different light irradiation (UVA and UVC) efficiencies; full equations and calculation details are provided in the Results and Discussion section of the SI.

Ion chromatography measurements

Ion chromatography (IC) was used to measure F^- concentration with a Metrohm 940 Professional IC Vario equipped with a Metrohm 919 autosampler and Metrosep A Supp 5 - 150/4.0 anion column. The F^- concentration in the supernatant was measured, and the percentage of defluorination was calculated based on the theoretical initial F^- concentration, which was determined from the initial PFAS concentrations obtained through LC-MS measurements. The calculation is provided in **Eq. 3** below[6].

$$overall\ deF\% = \frac{[F^-]}{[PFAS]_0 \times N_{C-F}} \times 100 \quad (3)$$

Where $[F^-]$ corresponds to the Fluoride molar concentration measured using IC, $[PFOA]_0$ corresponds to the initial PFAS molar concentration measured using LC-MS, and $N_{C\text{-}F}$ corresponds to the number of C-F bond exits in the structure of the used PFAS molecule.

^{19}F nuclear magnetic resonance analysis

Nuclear magnetic resonance (NMR) samples were prepared by sampling the reaction at delineated times, transferring 500 µL aliquots to new NMR tubes, and adding 10% D_2O to the NMR tube (for NMR deuterium lock). NMR spectra were recorded on an Agilent DD2 400 MHz spectrometer equipped with a OneNMR probe at 23 °C. Standard Agilent pulse sequences were employed. ^{19}F NMR spectra are reported in ppm. A spectral window with a range of -50 to -250 ppm was used. Following preliminary NMR scans, the 72 h samples were acidified (10 µL of 0.1 M HNO_3 were added to each NMR tube) to transform aqueous F^- into HF ($pK_a \approx 3.2$). The parameters of NMR analysis are outlined in **Table S1**. All ^{19}F NMR spectra processing was completed using MestreNova software. A detailed description of the methodology for referencing ^{19}F NMR spectra is provided in the Results and Discussion section of the SI and identified chemical shifts are tabulated in **Table S2**.

Quantitative liquid chromatography-mass spectrometry measurements

Mass spectrometric measurements were performed with a Shimadzu Scientific Instruments 8060 Triple-Quad liquid chromatography-mass spectrometry (LC-MS) system, equipped with a Nexera LC-40D xs UHPLC, consisting of a CBM-40 Lite system controller, a DGU-405 Degasser Unit, two LC-40D XS UHPLC pumps, a SIL-40C XS autosampler and a Column Oven CTO-40S. Mass spectra were subsequently recorded with the triple quadrupole (TQ) 8060 mass spectrometer. The samples were held at 20 ºC in the autosampler compartment after ultrasonification. 1 µL of each sample was injected into a sample loop and separated on a Shimadzu Velox PFPP column, 1.8 µL, 2.1x100 mm, equilibrated at 40 ºC in a column oven. A binary gradient was used during the measurements, respectively, Solvent A (Water, HPLC grade Chromasolv, with 0.1% Formic Acid) and Solvent B (MeOH, HPLC grade Chromasolv).

High resolution-mass spectrometry analysis

High-resolution mass spectrometric (HR-MS) measurements were conducted using a Shimadzu Scientific Instruments QToF 9030 LC-MS system, equipped with a Nexera LC-40D xs UHPLC setup identical to the one used in the quantitative LCMS analysis. For mass spectra recording, the quadrupole time-of-flight (QToF) 9030 mass spectrometer was employed. Samples were maintained at 4 °C within the autosampler compartment. A 1 µL aliquot of each sample was

injected into a sample loop and separated using a Shimadzu Velox PFPP column (1.8 µm, 2.1 x 100 mm), equilibrated at 40 °C in a column oven. A binary gradient was applied with Solvent A being water (HPLC grade Chromasolv) with 0.1% formic acid and Solvent B being acetonitrile (HPLC grade Chromasolv) with no additives. The flow rate was set at 0.250 mL/min, and the gradient composition varied as follows: from 0 to 2 min, 60% A and 40 % B; from 2 to 6.5 min, 15% A and 85% B; from 6.5 to 7.5 min, 15% A and 85% B; from 7.5 to 7.51 min, 60% A and 40% B; and from 7.51 to 10 min, 60% A and 40% B. The ionization source operated in electrospray ionization (ESI) mode with the electrospray needle at -3.0 kV. Nebulizer gas was set at 2 L/min, heating gas flow at 10 L/min, and the interface set at 300 °C. Dry gas was maintained at 10 L/min, with the desolvation line at 250 °C and the heating block at 400 °C. Mass spectra were acquired in the range of 50 to 1000 m/z in negative ion mode, while data-dependent MS/MS (DDA) fragmentation was performed in the range of 25 to 500 m/z with a collision energy spread of 40 ± 20 V (CE spread). Measurements and data post-processing were managed using LabSolutions 5.97 Realtime Analysis and PostRun software.

Results and Discussion

^{19}F NMR Methodology

Table S1. ^{19}F NMR experimental parameters

Summary of NMR Parameters		
Parameter	**Value**	**Unit**
Number of scans	3000	
Relaxation Delay	3	Seconds
Pulse Angle	90	Degrees
Acquisition Time	0.64	Seconds
Spectral Window	-50 to -250	ppm

Initial standardization of NMR spectra was conducted by adding trifluoroacetic acid (TFA, internal standard) to NMR tubes containing aliquots from 0 hour and 24 h samples. These experiments yielded a TFA CF_3 ^{19}F NMR shift at -77.10 and a PFOA CF_3 ^{19}F NMR shift at -82.40 ppm, matching those reported by Camdzic et al.[7], as well as an aqueous F^- shift around -121.44 ppm in the 24 h sample. After these initial tests, spectra within the dataset were standardized to one another using the 24 h sample as a reference as it contains signals of both starting material (PFOA at -82.40 ppm) and product (aqueous F^- at -121.44 ppm). Where observed, the PFOA CF_3 shift was referenced to -82.40 ppm[7] (observed in spectra of 0-hour, 8-hour, and 24-hour samples), while the aqueous F^- shift was referenced to -121.44 ppm (observed in spectra of 24-hour, 52-hour, and 72-hour samples). Aqueous F^- ^{19}F NMR shifts in the region of -121.44 ppm,[8, 9] and moreover a gap of roughly 41 ppm between PFOA CF_3 shifts and aqueous F^- shifts,[10] are in accordance with observations reported in the literature. The emergence of chemical shifts at -207.39 ppm in the 72 h samples indicates that HF is present in solution. Summary of mentioned chemical shifts can be found in **Table S2**.

Table S2. Summary of ^{19}NMR chemical shifts

Fluorinated Fragment	Chemical Shift (ppm)	Literature Report of a Similar Chemical Shift
TFA CF_3 (Internal Standard)	-77.10	Camdzic et al. **2023**[7]
PFOA CF_3	-82.40	Camdzic et al. **2023**[7]
PFOA αCF_2	-119.10	Lewis et al. **2023**[11]
F^-	-121.44	Bhat et al. **2022**,[8] Gerken **2011**,[9] Heerah et al. **2020**[10]
PFOA Interior CF_2	-123.47 to -127.70	Camdzic et al. **2021**[12]
H-F	-207.39	Dungan et al. **1970**[13]

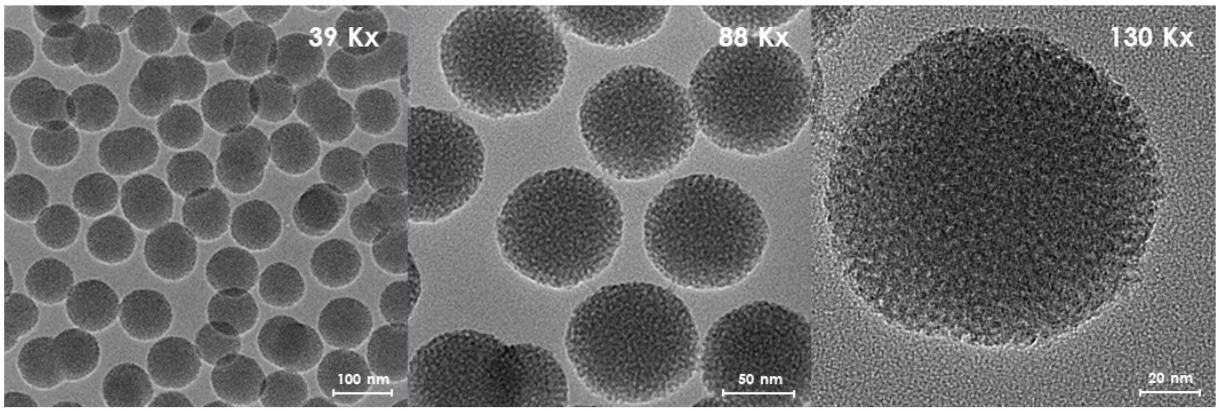

Fig. S1. TEM imaging of MSN particles at the magnifications of 39, 88, and 130 Kx.

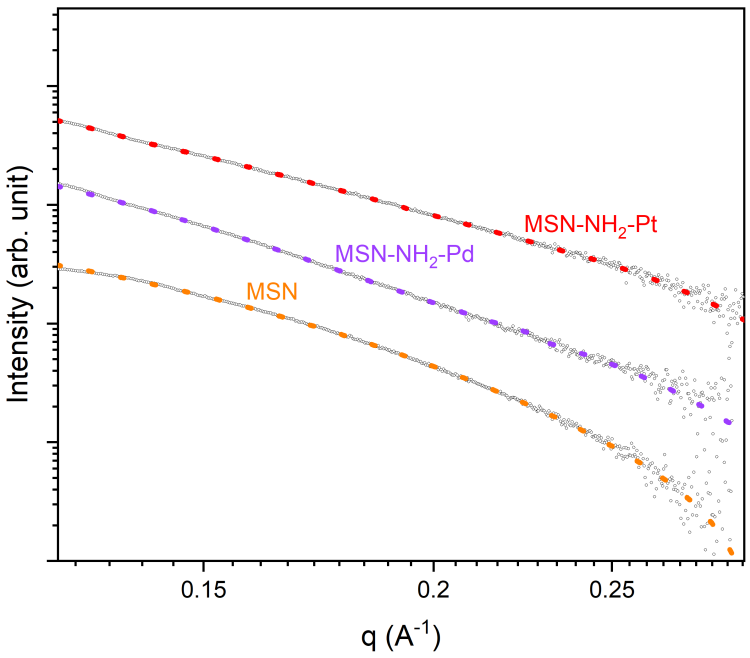

Fig. S2. SAXS analysis of MSN, MSN-NH_2-Pd and MSN-NH_2-Pt nanoparticles using Guinier−Porod model. The radius of gyration (R_g) of MSN pore is ca. 1.7 nm and this pore size shows up for both MSN-NH_2-Pd and MSN-NH_2-Pt samples. Strong X−ray scattering was found at *q* of 0.22−0.25 $Å^{-1}$ for both Pd and Pt nanoparticles embedded MSN samples, corresponding to R_g of 1.0 nm for Pd nanoparticles and 0.9 and 2.2 nm for Pt nanoparticles, respectively.

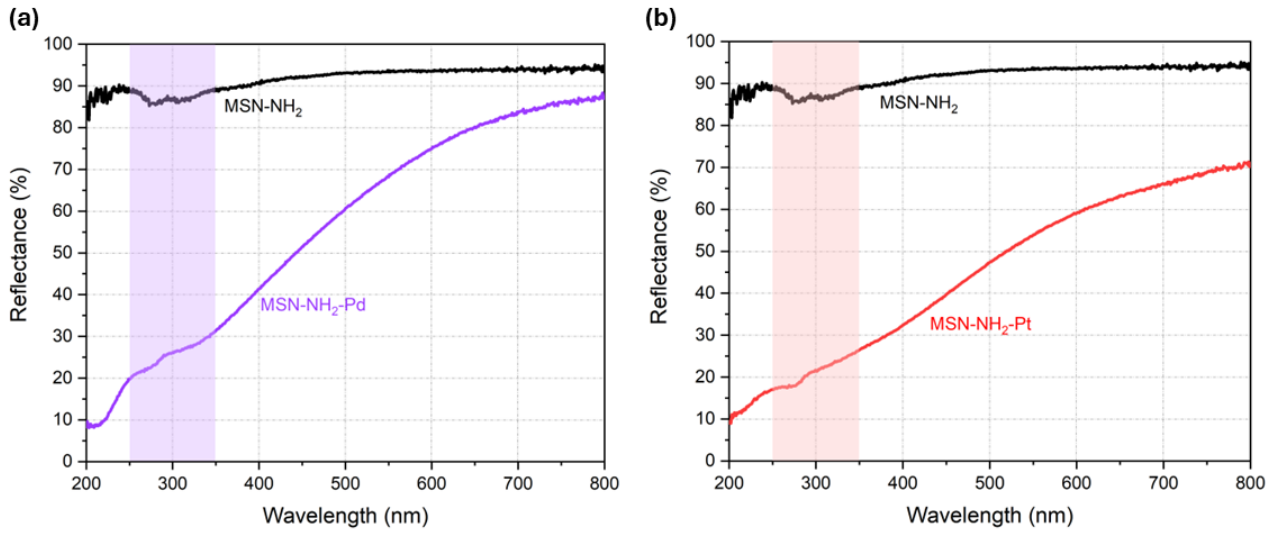

Fig. S3. UV-Vis DRS spectra of plasmonic photocatalysts (a) MSN-NH_2-Pd and (b) MSN-NH_2-Pt. The absorption band of MSN-NH_2-Pd is observed in the ~250–350 nm region (shaded purple in panel a), while the absorption band of MSN-NH_2-Pt appears in the ~250–350 nm region (shaded red in panel b).

Table S3. Reaction kinetics for control experiments.

Conditions									
Catalyst	**Compound**	**Scavenger**	**CO_2**	**H_2**	**Irradiation**	**pH**	**First-Order Pseudo Reaction Rate (h^{-1})**	**R^2**	**Percent Removal (%)**
Blank	PFOA	MeOH	✓	✗	UVC	4.2-4.5	0.0077	0.97	15.6
Blank	PFOA	MeOH	✓	✓	UVC	4.2-4.5	0.0075	0.97	16.3
Blank	PFOS	MeOH	✓	✗	UVC	4.2-4.5	0.0062	0.97	10
MSN-Pd	PFOA	MeOH	✓	✗	Dark	4.2-4.5	0.012	0.94	19
MSN-Pd	**PFOA**	**MeOH**	**✓**	**✗**	**UVC**	**4.2-4.5**	**0.34**	**0.94**	**99.1**
MSN-Pd	PFOA	Isopropanol	✓	✗	UVC	4.2-4.5	0.24	0.97	88
MSN-Pd	PFOA	TBA	✓	✗	UVC	4.2-4.5	0.25	0.95	98.7
MSN-Pd	PFOA	✗	✓	✗	UVC	4.2-4.5	0.14	0.97	62.5
MSN-Pd	PFOA	$AgNO_3$	✓	✗	UVC	4.2-4.5	0.02	0.85	25
MSN-Pd	PFOA	SOD + MeOH	✓	✗	UVC	4.2-4.5	0.25	0.94	88.9
MSN-Pd	PFOA	EDTA	✓	✗	UVC	4.2-4.5	0.08	0.95	60.2
MSN-Pd	PFOA	MeOH	✓	✓	UVC	4.2-4.5	0.21	0.98	99.2
MSN-Pd	PFOA	MeOH	✗	✗	UVC	6.8-7.2*	0.25	0.99	44.5
MSN-Pd	PFOA	MeOH	✗	✗	UVC	9.2**	0.048	0.99	41.1
MSN-Pd	PFOA	MeOH	✓	✗	UVA	4.2-4.5	0.08	0.98	67.9
MSN-Pd	**PFOS**	**MeOH**	**✓**	**✗**	**UVC**	**4.2-4.5**	**0.27**	**0.85**	**98.7**
MSN-Pd	PFOS	MeOH	✓	✗	UVA	4.2-4.5	0.1	0.97	81.3
MSN-Pt	**PFOA**	**MeOH**	**✓**	**✗**	**UVC**	**4.2-4.5**	**0.25**	**0.98**	**99**
MSN-Pt	PFOA	MeOH	✓	✗	UVA	4.2-4.5	0.03	0.95	74.1
MSN-Pt	**PFOS**	**MeOH**	**✓**	**✗**	**UVC**	**4.2-4.5**	**0.37**	**0.94**	**99.9**
MSN-Pt	PFOS	MeOH	✓	✗	UVA	4.2-4.5	0.02	0.87	68.8

*DI water without a buffer.
**Bicarbonate buffer.

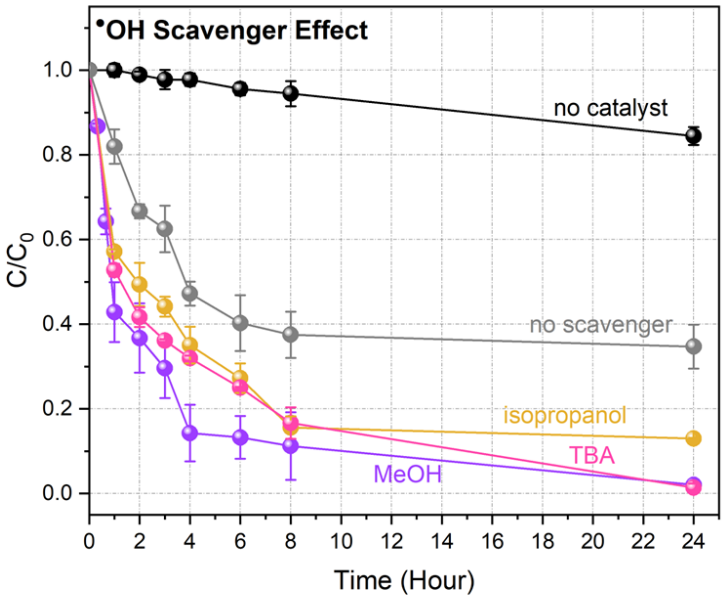

Fig. S4. Hydroxyl scavenger-dependent performance of MSN-NH_2-Pd particle under constant UVC irradiation with CO_2 applied and no external H_2 source. Associated reaction constants are given as $k_{OH,MeOH} = \sim 9.0 \times 10^8\ M^{-1} \cdot s^{-1}$, $k_{OH,TBA} = \sim 6.2 \times 10^8\ M^{-1} \cdot s^{-1}$, and $k_{OH,isopropanol} = \sim 2.0 \times 10^9\ M^{-1} \cdot s^{-1}$)[14].

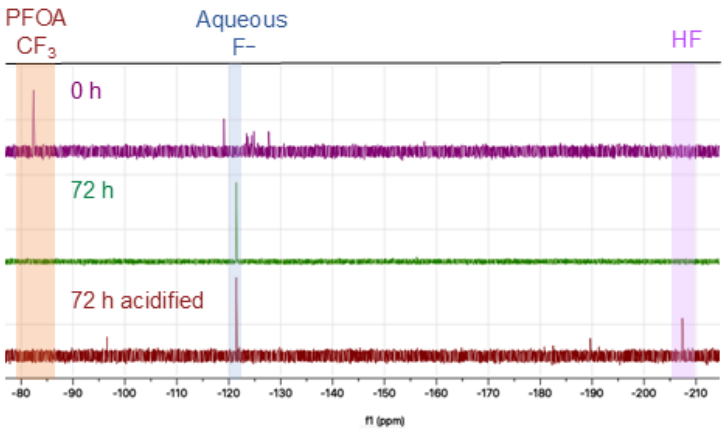

Figure S5. ^{19}F NMR spectra of aliquots of 0 h, 72 h, and acidified 72 h samples throughout the reductive defluorination reaction with plasmonic photocatalyst MSN-NH_2-Pd under constant UVC irradiation with MeOH scavenger and CO_2 applied at pH 4.2-4.5.

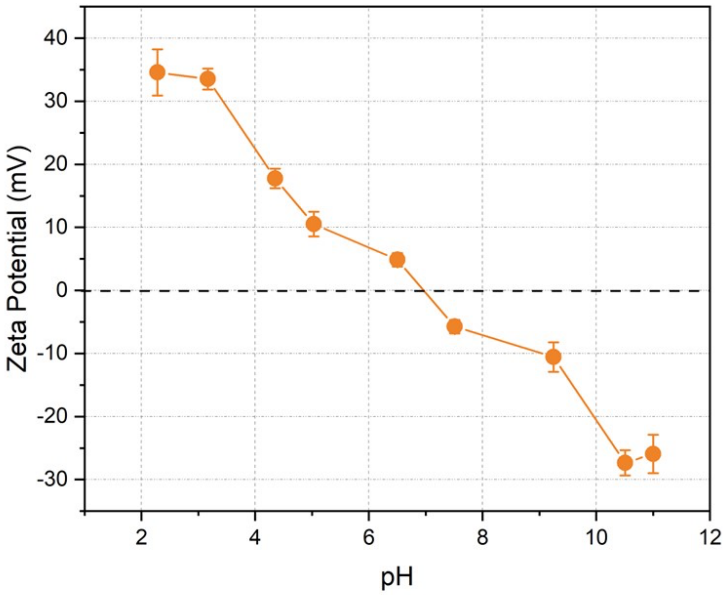

Fig. S6. Zeta potential of MSN-NH_2-Pd particles across a pH range of 2 to 11.

Sorption Experiments

Table S4. Parameters for Langmuir and Freundlich fits of relevant nanoparticles, including approximate maximum adsorption capacity q_{max} (mg/g); Langmuir constant b (L/mg); Freundlich constants associated with adsorption capacity K_f ((mg/g) $(L/mg)^{1/n}$) and adsorption intensity n (unitless); R^2 value for each model; half-concentration constant $C_{1/2}$ (mg/L or ppm), and equilibrium states for conditions of 10 ppm initial PFAS concentration and 2 g/L nanomaterial, C_{10} (ppm) and q_{10} (mg/g).

Isotherm Model	**MSN-NH_2-Pd**	**MSN-NH_2-Pt**	**MSN-NH_2-Pd**	**MSN-NH_2-Pt**
	PFOA		**PFOS**	
Langmuir Isotherm $q_e = \frac{q_{max} b C_e}{1+bC_e}$				
$\mathbf{q_{max}}$	126.70	75.97	52.02	81.20
b	2.45E-3	0.47	0.01	1.72
$\mathbf{R^2}$	0.87	0.97	0.98	0.98
$\mathbf{C_{1/2}}$	408.16	2.11	109.65	0.58
Freundlich Isotherm $q_e = K_f {C_e}^n$				
$\mathbf{K_f}$	8.21E-3	24.08	2.07	42.16
n	1.62	0.26	0.53	0.42
$\mathbf{R^2}$	0.97	0.90	0.98	0.99
$\mathbf{q_{max}}$	69.86	74.79	~35.00	79.00
$\mathbf{C_{1/2}}$	171.68	5.36	3.09	0.97
Experimental Conditions				
$\mathbf{C_{10}}$	6	0.2	1.77	0.016
$\mathbf{q_{10}}$	3.02	6.78	2.96	4.13
$\mathbf{K_d}$	0.5	33.9	1.67	258.12

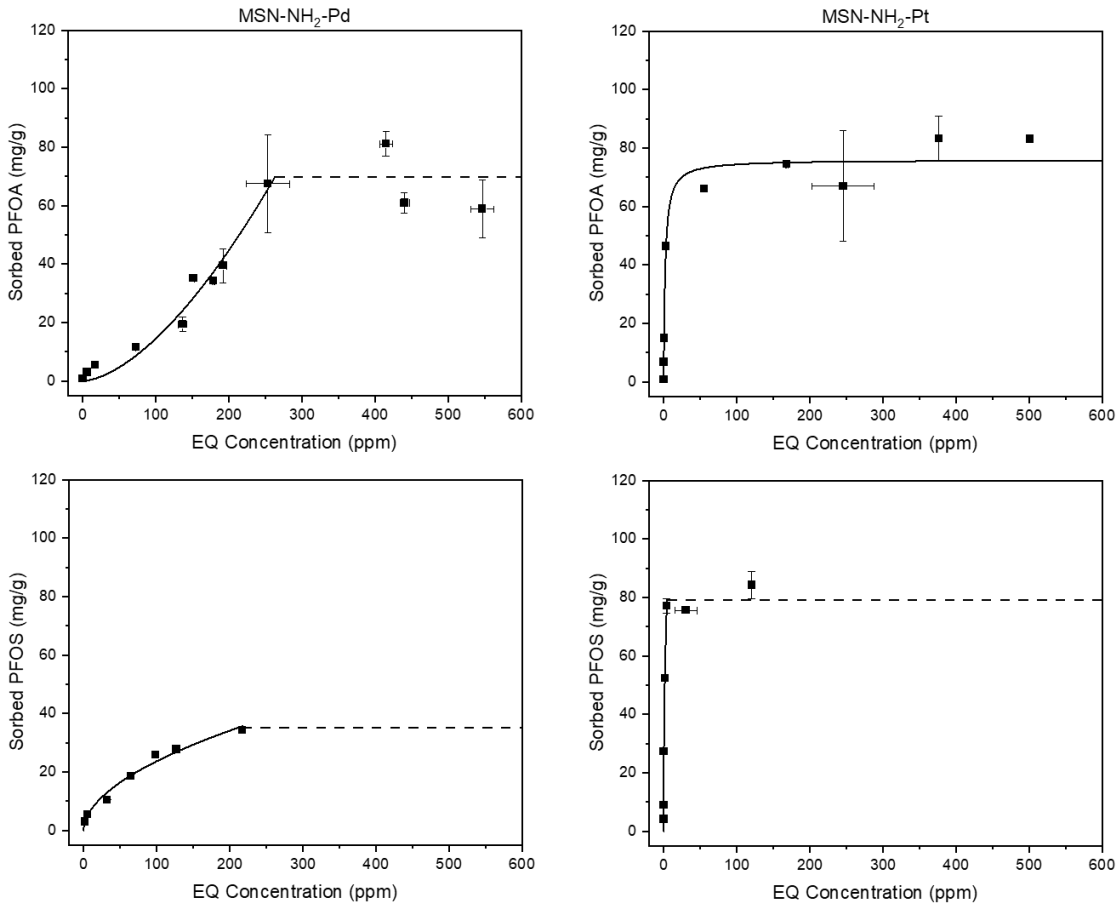

Figure S7. Best-fit sorption isotherms for PFOA and PFOS adsorption to MSN-NH_2-Pd and MSN-NH_2-Pt. PFOA sorption to MSN-NH_2-Pt fit a Langmuir isotherm best; all other circumstances are best modeled by a Freundlich isotherm. Sorption experiments were performed with 2 g/L sorbent concentrations, in 1-500 ppm PFAS solutions at pH 4 without pH adjustment. Full experimental details are provided methods section.

Sorption isotherms of best fit can be seen above in **Figure S7**. PFOA adsorption on MSN-NH_2-Pd is characterized by a Freundlich isotherm with an n-value greater than 1, demonstrating a possible co-sorption effect at increasing solution concentrations until the material surface is saturated. Freundlich isotherms are commonly used for materials with heterogeneous surfaces, where contaminant adsorption occurs at sites with varying interaction energies. PFOA adsorption on MSN-NH_2-Pt, by contrast, can be best characterized by a Langmuir isotherm. Langmuir isotherms typically describe homogeneous material surfaces, where the contaminant interacts with all adsorption sites with approximately equal energy. PFOS adsorption on both MSN-NH_2-Pd and MSN-NH_2-Pt can be characterized by Freundlich isotherms with n-values less than one, which indicates that adsorption becomes less favorable as the surface of the material is saturated. Notably,

MSN-NH_2-Pt has relatively similar adsorption capacities for both PFOA and PFOS (by mass) whereas, MSN-NH_2-Pd has a higher adsorption capacity for PFOA than for PFOS. However, in the case of MSN-NH_2-Pd, PFOS has a much lower half-saturation constant, indicating that PFOS may sorb more readily at low concentrations but block available adsorption sites at higher concentrations. Under equilibrium conditions with 10 ppm initial PFAS concentration and 2 g/L nanomaterial, sorption behavior varied across PFAS type and plasmonic photocatalyst. For PFOA, the distribution coefficient (K_d) was 0.5 for MSN-NH_2-Pd and 33.9 for MSN-NH_2-Pt, while for PFOS, K_d was 1.67 for MSN-NH_2-Pd and significantly higher at 258.1 for MSN-NH_2-Pt. These values reflect the amount adsorbed per gram of sorbent (q_{10}) relative to the remaining equilibrium concentration in solution (C_{10}).

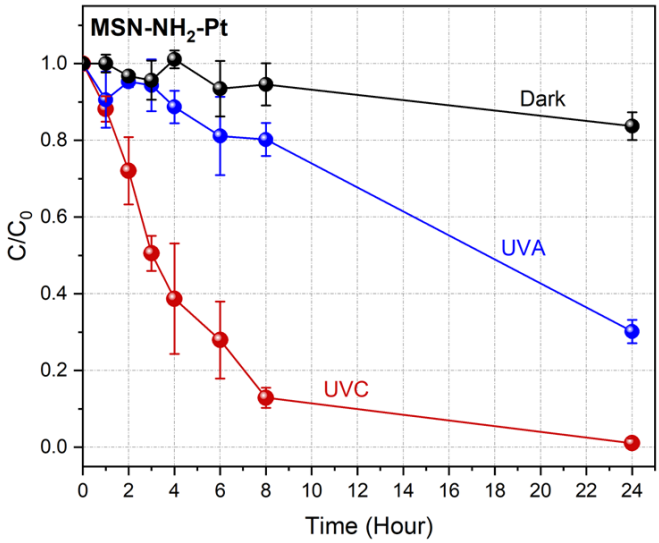

Fig. S8. Irradiation-dependent performance of MSN-NH_2-Pt particle for PFOA degradation under constant UVC/A irradiation with MeOH and CO_2 applied.

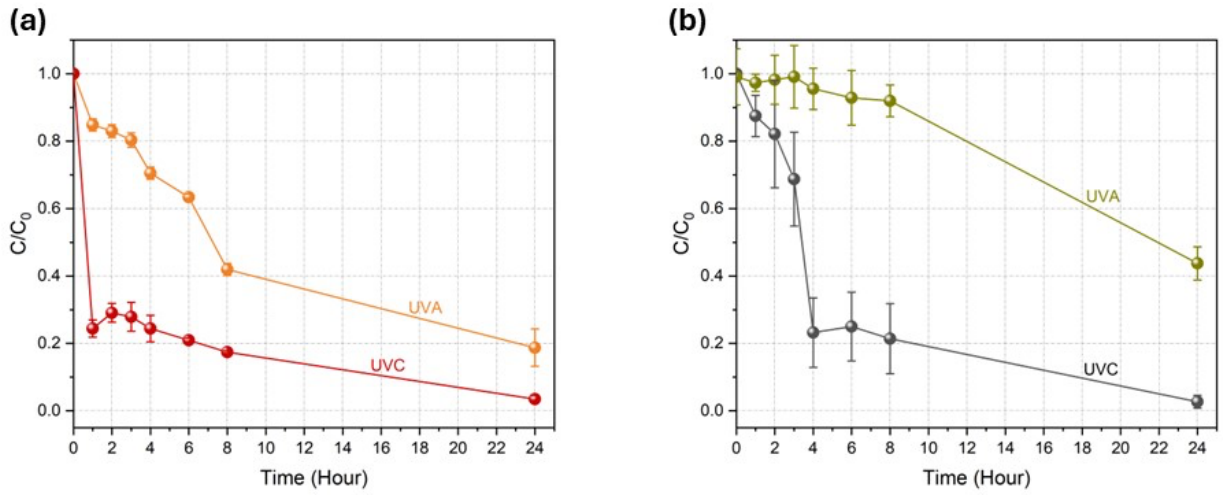

Fig. S9. (a) Irradiation dependent performance of MSN-Pd particle for PFOS degradation under constant UVC/A irradiation with methanol scavenger and CO_2 applied. (b) Irradiation dependent performance of MSN-Pt particle for PFOS degradation under constant UVC/A irradiation with methanol scavenger and CO_2 applied.

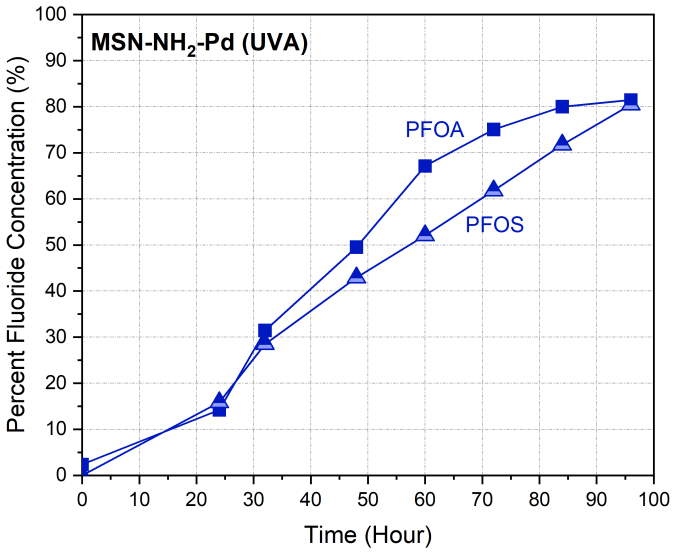

Fig. S10. Percent fluoride release (quantified via IC) over 96 h for MSN-NH_2 during PFOA and PFOS degradation under constant UVA irradiation with 20 ppm MeOH ($^{\bullet}$OH scavenger) and CO_2 at pH 4.2–4.5 at room temperature. All experiments used 10 ppm PFAS (quantified via LC-MS) and 400 ppm photocatalyst (40 mg).

Photon flux calculations

Photon flux (ϕ) represents the number of incident photons per unit area per unit time and is crucial in photochemical and plasmonic reactions, as it dictates the availability of photons to drive catalytic processes. For this calculation, our photon flux normalization was based on the dominant emission lines of each lamp, and 100% light absorption was assumed. Light intensities were measured with UVP model UVX portable digital radiometer W/UVX-36. The photon flux was calculated using the equation:

$$\phi = \frac{I \times \lambda}{h \times c}$$

where:

- I is the light intensity in **W/m²** (converted from mW/cm² by multiplying by 10)
- λ is the wavelength in **meters**
- h = 6.626×10^{-34} J/s is Planck's constant
- c = 3.0×10^{8} m/s is the speed of light

From the given light intensities of the light sources:

- **UVC (254 nm, 2.6 mW/cm²)** → Photon flux: **3.3×10^{19} photons/s·m²**
- **UVA (368 nm, 7.3 mW/cm²)** → Photon flux: **1.3×10^{20} photons/s·m²**

Normalization of Reaction Rates by Photon Flux

To directly compare the efficiency of UVA and UVC irradiation, the reaction rates were normalized by dividing by the corresponding photon flux:

$$k_{normalized} = \frac{k}{\phi}$$

The results are given in **Table S5** below.

Table S5. The resulting normalized reaction rates ($\times 10^{-20}$ h^{-1} per photon flux (photons/s·m²))

Light Source	Compound	MSN-NH_2-Pd	MSN-NH_2-Pt
UVC	PFOA	1.1	0.8
UVC	PFOS	0.8	1.1
UVA	PFOA	0.06	0.02
UVA	PFOS	0.08	0.02

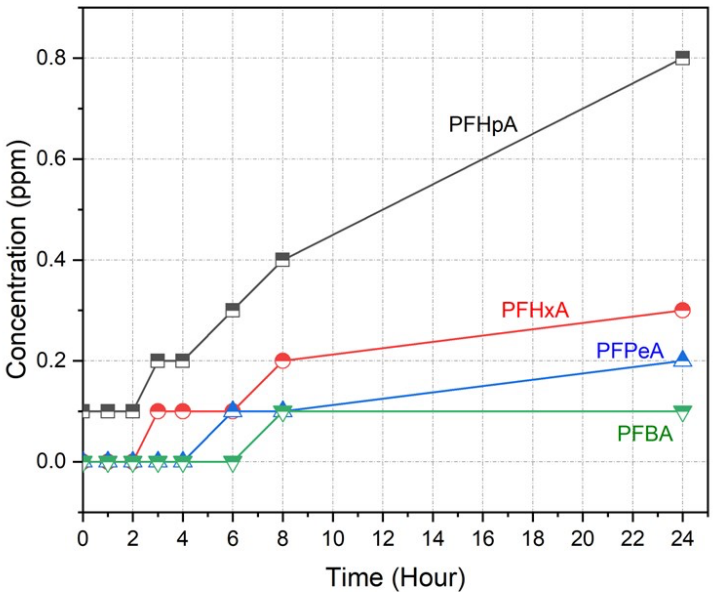

Fig. S11. Quantitative LC-MS concentration results for different chain PFAS species (PFHpA: perfluoroheptanoic acid; PFHxA: perfluorohexanoic acid; PFPeA: perfluoropentanoic acid; PFBA: perfluorobutanoic acid) after the photocatalytic degradation of 8C chain PFOA with plasmonic photocatalyst MSN-NH_2-Pd catalyst under UVC irradiation with CO_2 applied at pH 4.2-4.5 and without the use of a reactant scavenger.

LSPR-driven hydrogen generation

In the case of reductive PFAS defluorination, for each fluorine atom removed through a reductive reaction, a hydrogen atom is required[15]. For systems studied here, a control experiment was performed without UV irradiation (under dark conditions at pH 4.2–4.5 with only 400 ppm catalysts, 10 ppm PFAS, 20 ppm MeOH, and an external hydrogen source bubbled with 10 scfm) with no PFAS transformation observed, as illustrated in **Fig. S13**.

As reported by others, PNPs can catalyze water-splitting reactions, suggesting water splitting as a possible side reaction occurring during the degradation process[16-18]. Additionally, e_{aq}^- can react with H^+ (coming from **Eq. 4**) and yield a conjugate acid $H^\bullet$ which can subsequently react with e_{aq}^- to produce molecular hydrogen as in **Eq. 4**[3]. Another possible route involves the direct combination of e_{aq}^- to form hydrogen and OH^- as in **Eq. 5**[3].

$$e_{aq}^- + H^\bullet + H_2O \rightarrow H_2 + OH^- \quad (4)$$

$$e_{aq}^- + e_{aq}^- + 2H_2O \rightarrow H_2 + 2OH^- \quad (5)$$

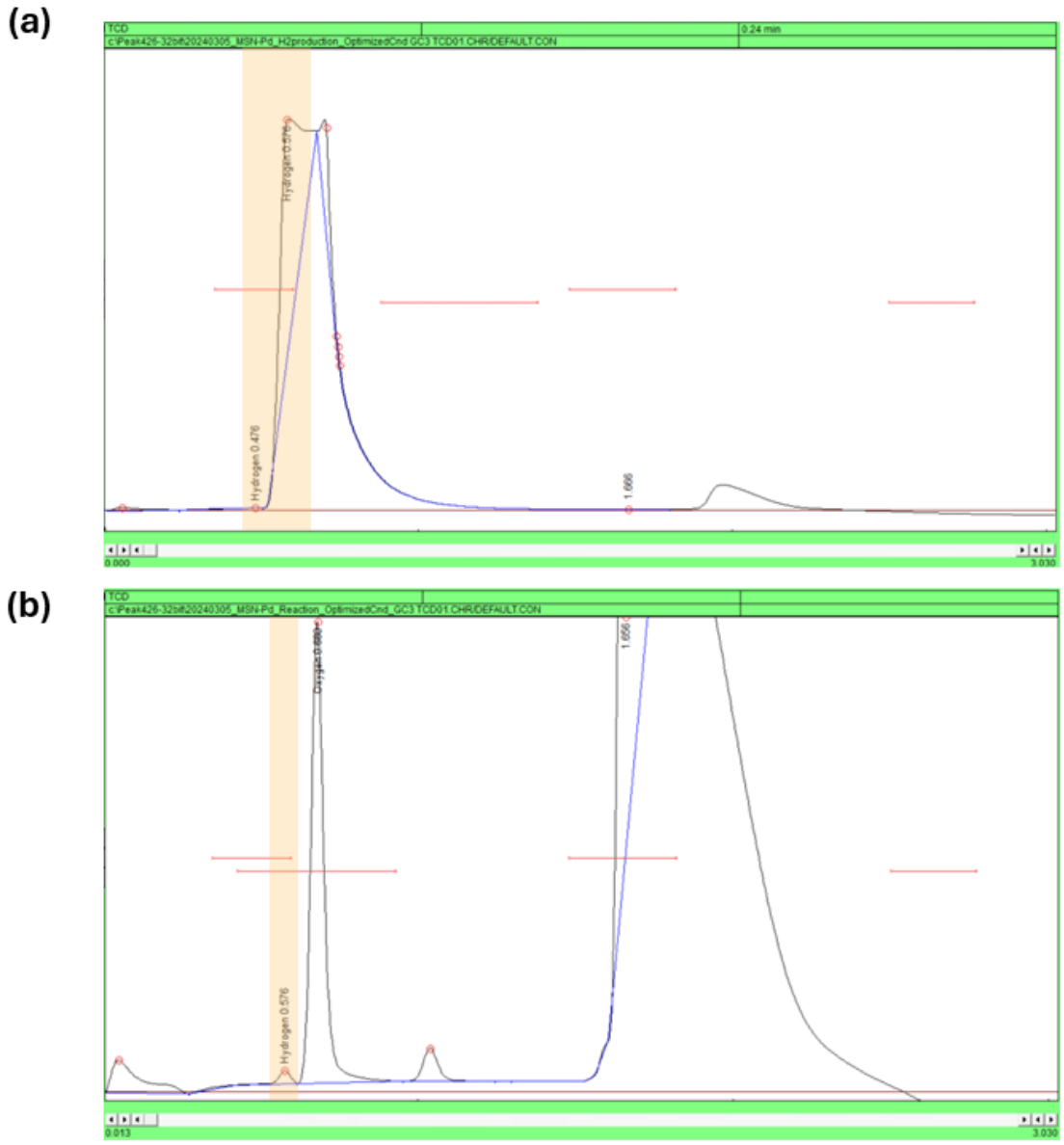

Fig. S12. (a) GC-MS results for hydrogen detection using MSN-Pd particle under constant UVC irradiation with methanol scavenger and no H_2 applied in the absence of PFOA. **(b)** GC-MS results for hydrogen detection using MSN-NH_2-Pd particle under constant UVC irradiation with methanol scavenger and no H_2 applied in the presence of PFOA.

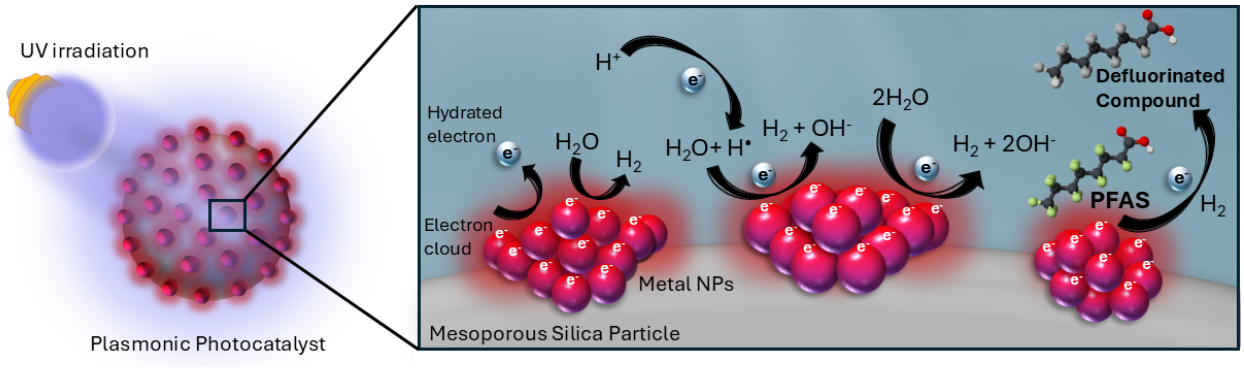

Fig. S13. Schematic illustration of plasmon-induced side reactions on plasmonic photocatalysts. Diagram depicting the plasmon-driven reaction mechanisms occurring at the active sites of MSN-NH_2-Pd and MSN-NH_2-Pt photocatalysts, which facilitate hydrogen generation as part of the reaction process.

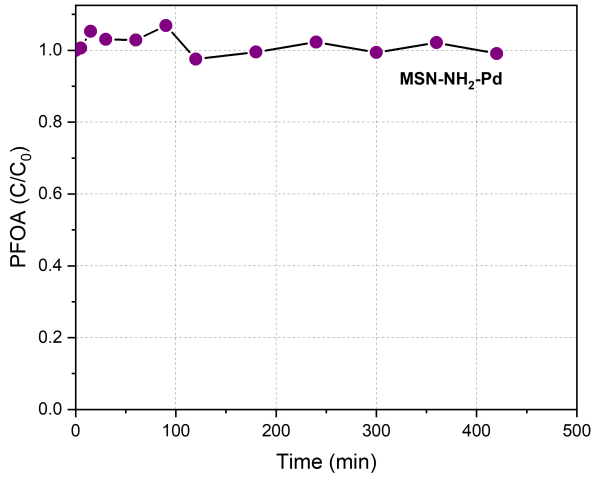

Fig. S14. Obtained quantitative LC-MS concentration result for 8C chain PFOA with plasmonic photocatalyst MSN-NH_2-Pd catalyst under dark conditions with CO_2 applied at pH 4.2-4.5 involving 400 ppm catalysts, 10 ppm PFAS, 2.5 mL MeOH, and an external hydrogen source bubbled with 10 scfm.

Mechanistic discussion for side reactions involved in PFOA degradation

In addition to C8 defluorinated intermediate products discussed in the main text, (significantly) lower-intensity intermediates of various perfluoroalkyl structures were also detected through LC-HR-MS/MS analysis, indicating a series of radical-mediated structural degradation, H/F exchange, and fluoride removal side reactions happening subsequently and in parallel with the major reductive defluorination pathways. Such partially defluorinated perfluoroalkyl compounds (C8-C5) are observed, including C7 perfluoroalkyl compounds having no (carboxylic) functional head group (*e.g.*, $C_7F_{13}^-$, $C_7F_{12}H$, $C_7F_{11}^-$, $C_7F_{10}H^-$, $C_7F_9^-$, and $C_7F_7^-$)**,** with correlations in their corresponding HR-MS chromatographs (**Fig. S14-S16**) to illustrate possible side reactions. Notably, perfluoroalkyl compounds without a functional head group are not commonly reported as intermediate products in conventional reductive and oxidative pathways, highlighting the distinctive/unique nature of this pathway. Interestingly, data also indicates a possible formation of a double bond within the carbon chain of the fluorocarbon tail following the removal of HF or F_2 fragments (the nature of this fragmentation will be explored in the later stages of the research). As a starting point, a similar phenomenon was observed in a computational study on PFOA defluorination, where the addition of multiple electrons to PFAS resulted in two distinct spin-density evolutions — trans-type or cis-type elimination — depending on the dissociation of fluorine atoms from the carbon backbone structure[19]. It was reported that a trans-type elimination is suggested to be central to PFAS degradation, as it leads to the formation of C=C bonds, which are more susceptible to defluorination[19]. This finding is supported by other experimental studies showing easier dissociation of fluorine atoms attached to C=C bonds compared to C−C bonds[20, 21]. Additionally, the formation of HF molecules during the simulations aligned with our NMR results shown in **Fig. S5**. Consequently, results may suggest that plasmon-driven excess electrons can create distinct spin-density evolutions on perfluoroalkyl radicals to facilitate the loss of fluorine fragments from the fluorocarbon tail.

As part of intermediate product identification, short(er)-chain perfluoroalkyl radicals (*e.g.*, $C_6F_{13}^-$, $C_4F_9^-$, $C_3F_5^-$, $C_2F_5^-$, CF_3^- **Fig. S16 and Table S6**) were also detected. Interestingly, such intermediate structures are similar to those observed via thermal degradation of PFOA, where decarboxylation (loss of the head group) is followed by chain shortening through C−C bond cleavage[22-24]. For these, the concurrent presence of both HF and free F^- was also observed via ^{19}F NMR analysis (**Fig. S5**)**,** which is consistent with experimental and computational studies on

thermal degradation[22-24]. Based on these data and other reports, it might be hypothesized that the PNP sites on plasmonic photocatalysts likely also facilitate thermal degradation-like reactions through plasmon-induced hot electron formation (the nature of this thermal degradation-like reactions will be explored in the later stages of the research)[25-29]. The non-radiative decay of excited surface plasmons generates energetic hot charge carriers, which can be transfered to adsorbate molecules, initiating chemical reactions, and enabling/enhancing C–C bond cleavage, consistent with plasmon-driven photothermal reactions[27-29]. It is noteworthy to mention that these byproducts were detected at markedly lower intensities than the major H/F exchange intermediates, indicating they likely originate from concurrent but relatively minor side reactions under the same reaction conditions.

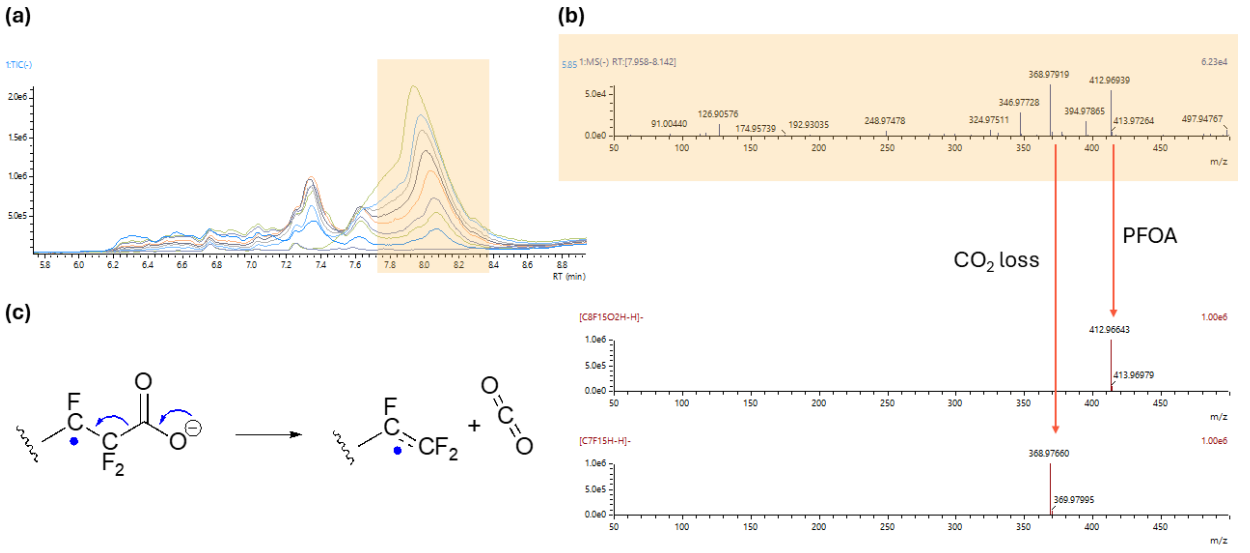

Fig. S15. (a) LC-HR-MS/MS chromatogram for different time samples for e_{aq}^--mediated decarboxylation of PFOA during reductive defluorination with plasmonic photocatalyst MSN-NH_2-Pd catalyst under optimized conditions. (b) LC-HR-MS/MS chromatogram peak assignments for intermediate product identification. (c) Possible alternative mechanism for CO_2 loss indicating the C–C sigma bond cleavage balanced by the new C–O π bond and the half π bond in the possible product alkene radical anion (e^- in the π*).

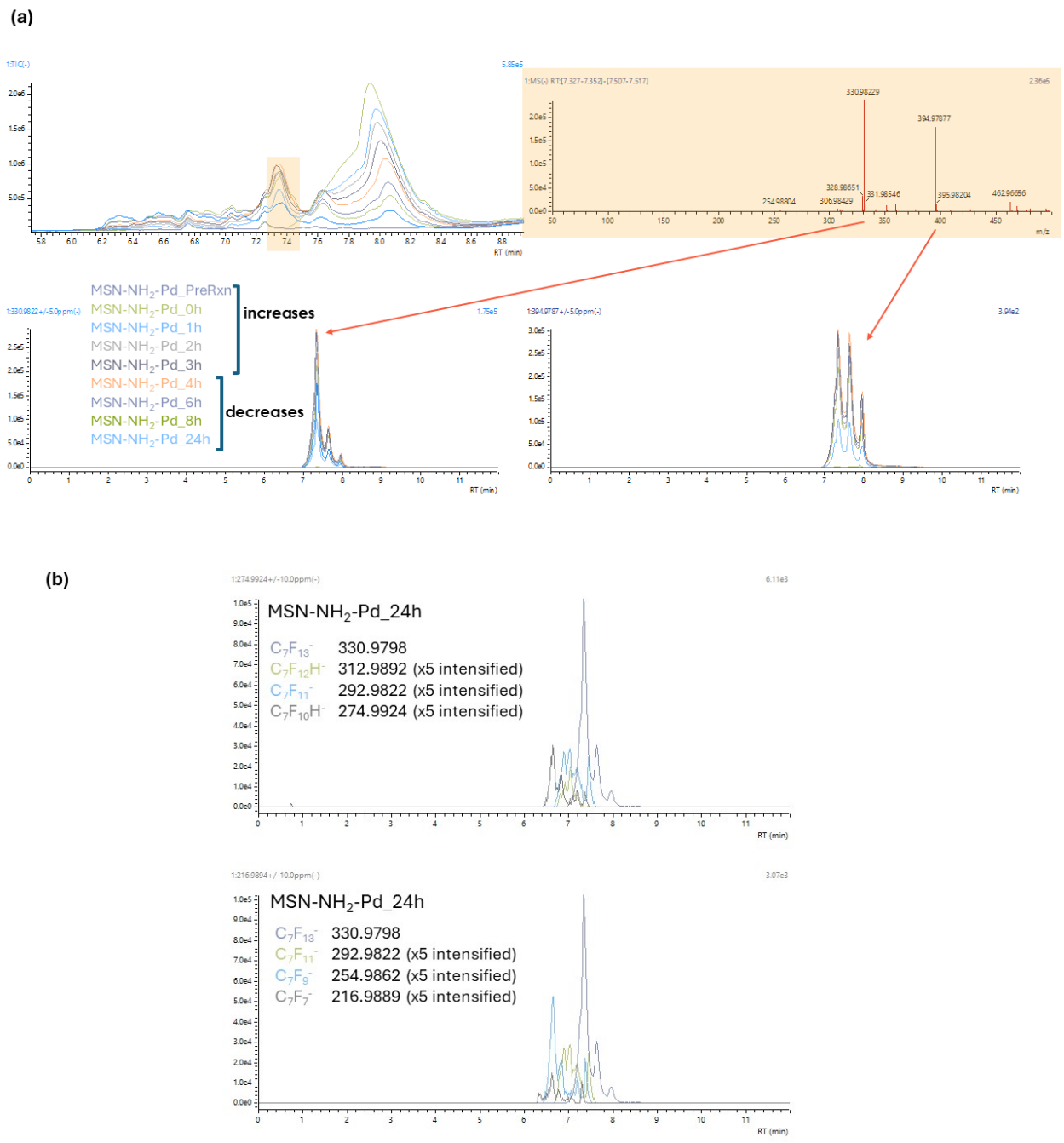

Fig. S16. LC-HR-MS/MS analysis of reaction samples for intermediate product identification for the 24h sample. (a) Mass identification showing the formation and disappearance of partially defluorinated ($C_7F_{14}HCOO^-$, *m/z* 394.9756) and C7 perfluoroalkyl ($C_7F_{13}^-$, *m/z* 330.9798) intermediate compounds. (b) Mass identification showing the formation and disappearance of intermediate perfluoroalkyl compounds. The initial LC-HR-MS/MS analysis was conducted using a different binary gradient ratio, with Solvent A consisting of HPLC-grade water (Chromasolv) containing 0.1% formic acid, and Solvent B consisting of HPLC-grade methanol (Chromasolv).

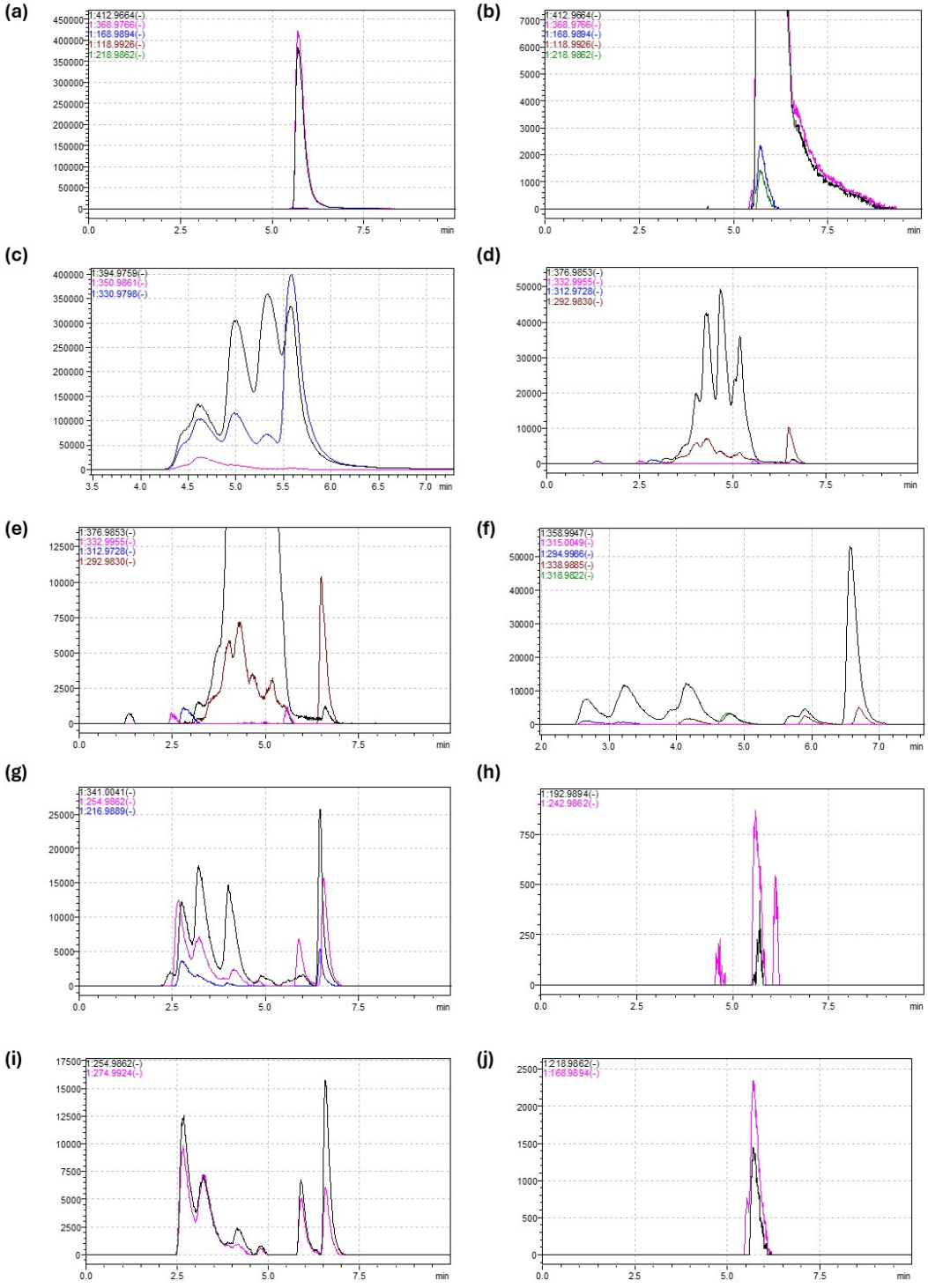
(a)
1:412.9664(-)
1:368.9766(-)
1:168.9894(-)
1:118.9926(-)
1:218.9862(-)
(b)
1:412.9664(-)
1:368.9766(-)
1:168.9894(-)
1:118.9926(-)
1:218.9862(-)
(c)
1:394.9759(-)
1:350.9861(-)
1:330.9798(-)
(d)
1:376.9853(-)
1:332.9955(-)
1:312.9728(-)
1:292.9830(-)
(e)
1:376.9853(-)
1:332.9955(-)
1:312.9728(-)
1:292.9830(-)
(f)
1:358.9947(-)
1:315.0049(-)
1:294.9986(-)
1:338.9885(-)
1:318.9822(-)
(g)
1:341.0041(-)
1:254.9862(-)
1:216.9889(-)
(h)
1:192.9894(-)
1:242.9862(-)
(i)
1:254.9862(-)
1:274.9924(-)
(j)
1:218.9862(-)
1:168.9894(-)
min

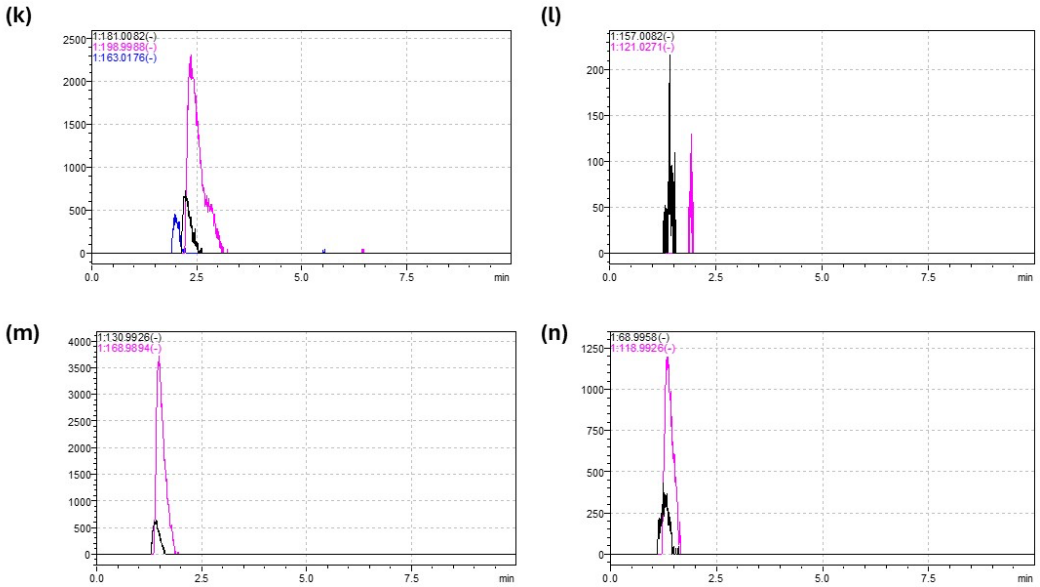

Fig. S17. HR-MS chromatograms showing corresponding identification and correlation of found intermediate compounds. (a-b) Identification and correlation of PFOA (*m/z* 412.9664), $C_7F_{15}^-$ (*m/z* 368.9766), $C_4F_9^-$ (*m/z* 218.9862), $C_3F_7^-$ (*m/z* 168.9894), and $C_2F_5^-$ (*m/z* 118.9226). (c) Identification of four PFOA(1H) (*m/z* 394.9759) isomers and their correlation with corresponding perfluoroalkyl compounds $C_7F_{14}H^-$ (*m/z* 350.9861) and $C_7F_{13}^-$ (*m/z* 330.9798). (d-e) Identification of PFOA(2H) (*m/z* 376.9853) isomers and their correlation with corresponding perfluoroalkyl compounds $C_7F_{13}H_2^-$ (*m/z* 332.9954), $C_7F_{12}H^-$ (*m/z* 312.9892), and $C_7F_{11}^-$ (*m/z* 292.9822). (f) Identification of PFOA(3H) (*m/z* 358.9947) isomers and their correlation with corresponding perfluoroalkyl compounds $C_8F_{11}H_2O_2^-$ (*m/z* 338.9885), $C_8F_{10}HO_2^-$ (*m/z* 318.9822), $C_7F_{12}H_3^-$ (*m/z* 315.0049), and $C_7F_{11}H_2^-$ (*m/z* 294.9986). (g) Identification of PFOA(4H) (*m/z* 341.0041) isomers and their correlation with corresponding perfluoroalkyl compounds $C_7F_9^-$ (*m/z* 254.9862) and $C_7F_7^-$ (*m/z* 216.9889). (h) Identification and correlation of perfluoroalkyl compounds $C_6F_9^-$ (*m/z* 242.9862) and $C_5F_7^-$ (*m/z* 192.9894). (i) Identification and correlation of perfluoroalkyl compounds $C_7F_{10}H^-$ (*m/z* 274.9924) and $C_7F_9^-$ (*m/z* 254.9862). (j) Identification and correlation of perfluoroalkyl compounds $C_4F_9^-$ (*m/z* 218.9862) and $C_3F_7^-$ (*m/z* 168.9894). (k) Identification of perfluoroalkyl compounds $C_7F_6H^-$ (*m/z* 198.9982), $C_7F_5H_2^-$ (*m/z* 181.0076), and $C_6F_4H_3^-$ (*m/z* 163.0170). (l) Identification of perfluoroalkyl compounds $C_5F_5H_2^-$ (*m/z* 157.0082), $C_5F_3H_4^-$ (*m/z* 121.0271). (m) Identification and correlation of perfluoroalkyl compounds $C_3F_7^-$ (*m/z* 168.9894) and $C_3F_5^-$ (*m/z* 130.9926). (n) Identification and correlation of perfluoroalkyl compounds $C_2F_5^-$ (*m/z* 118.9226) and CF_3^- (*m/z* 68.9958).

HR-MS chromatogram from 6th hour:

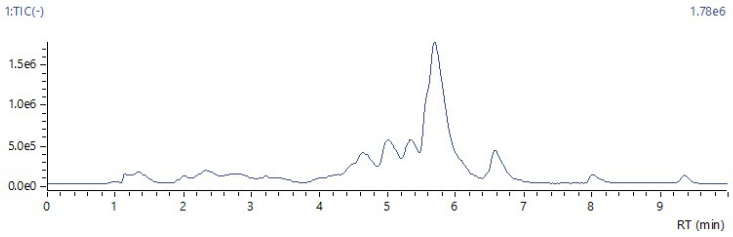

PFOA ($C_7F_{15}COO^-$)

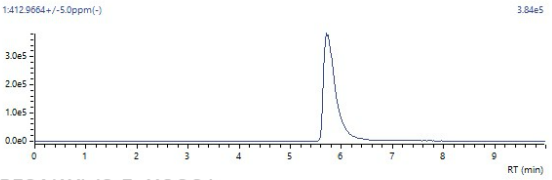

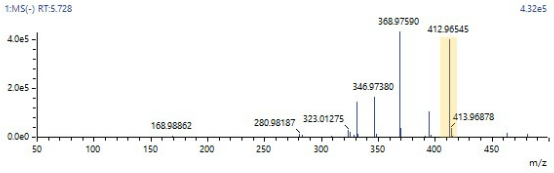

PFOA(1H) ($C_7F_{14}HCOO^-$)

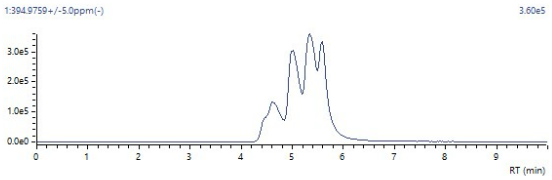

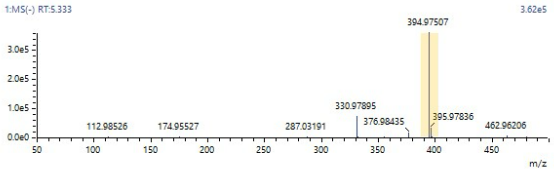

PFOA(2H) ($C_7F_{13}H_2COO^-$)

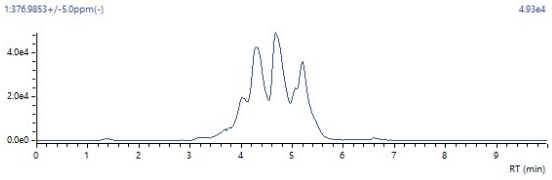

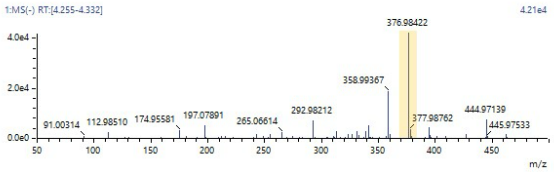

PFOA(3H) ($C_7F_{12}H_3COO^-$)

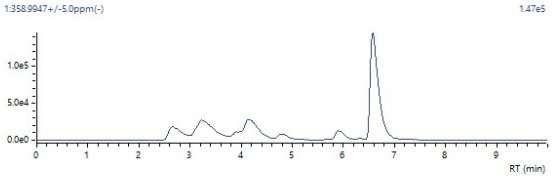

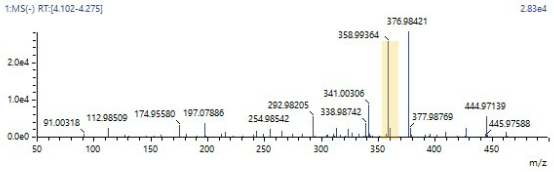

PFOA(4H) ($C_7F_{11}H_4COO^-$)

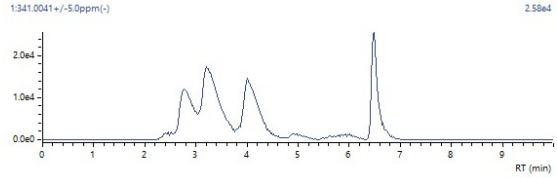

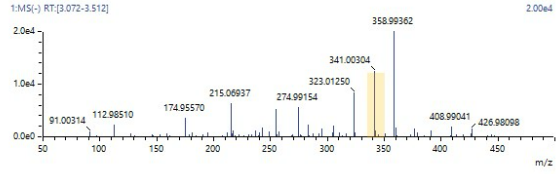

PFOA(5H) ($C_7F_{10}H_5COO^-$)

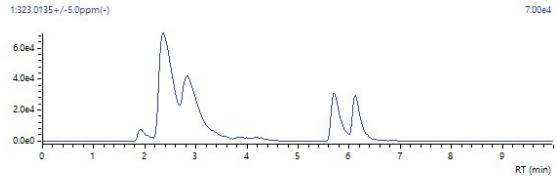

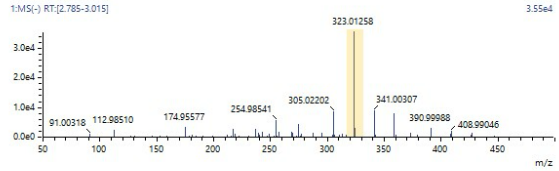

PFOA(6H) ($C_7F_9H_6COO^-$)

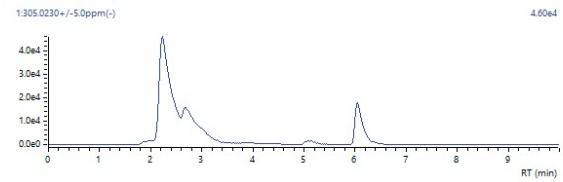

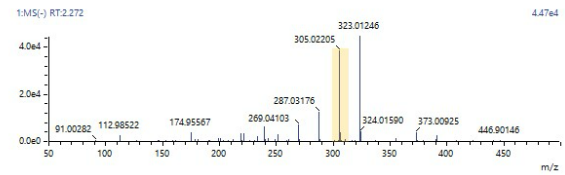

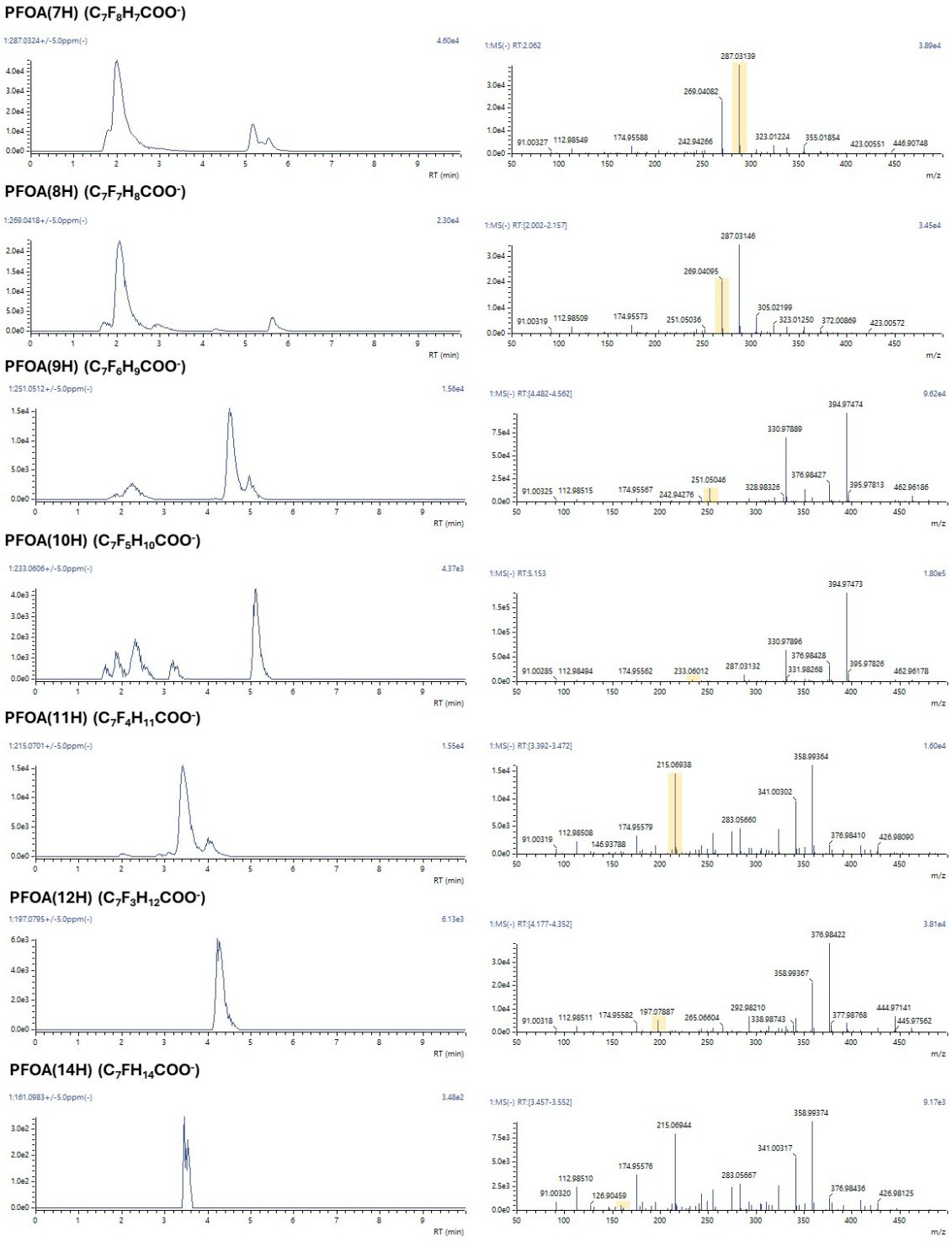

Fig. S18. HR-MS identification of defluorinated PFAS intermediates formed during e_{aq}^- mediated defluorination of PFOA with MSN-NH_2-Pd. Please see **Table S6** for associated retention times for each identified species.

Table S6. Mass-to-charge ratios and retention times of intermediates formed during e_{aq}^- mediated defluorination of PFOA with MSN-NH_2-Pd and identified via HR-MS.

Chemical Formula $[M-H]^-$	Mass-to-charge ratio (*m/z*)	Retention Time (t_R) (min)
$C_7F_{15}COO^-$	412.9664	5.71
$C_7F_{14}HCOO^-$	394.9759	5.57 – 5.31 – 4.97 – 4.59
$C_7F_{13}H_2COO^-$	376.9853	5.19 – 4.64 – 4.25 – 3.98
$C_7F_{12}H_3COO^-$	358.9947	6.55 – 4.16 – 3.23 – 2.67
$C_7F_{11}H_4COO^-$	341.0041	6.46 – 4.01 – 3.21 – 2.75
$C_7F_{10}H_5COO^-$	323.0135	6.12 – 5.69 – 2.83 – 2.36
$C_7F_9H_6COO^-$	305.0135	6.05 – 2.22
$C_7F_8H_7COO^-$	287.0324	5.14 – 2.05
$C_7F_7H_8COO^-$	269.0418	5.63 – 2.04
$C_7F_6H_9COO^-$	251.0512	4.49 – 2.24
$C_7F_5H_{10}COO^-$	233.0606	5.10 – 1.6 – 1.9 – 2.4 – 3.2
$C_7F_4H_{11}COO^-$	215. 0701	3.41
$C_7F_3H_{12}COO^-$	197.0795	4.23
$C_7FH_{14}COO^-$	162.0983	3.45
$C_7F_{14}H^-$	350.9869	4.655
$C_7F_{13}^-$	330.9798	5.613 – 5.345 – 5.007 – 4.650
$C_7F_{11}^-$	292.9830	4.332
$C_6F_9^-$	242.9862	5.618
$C_5F_7^-$	192.9894	5.708
$C_4F_5^-$	142.9926	1.498
$C_7F_{13}H_2^-$	332.9954	4.330
$C_7F_{12}H^-$	312.9893	4.015
$C_8F_{11}H_2O_2^-$	338.9885	6.743
$C_8F_{10}HO_2^-$	318.9822	6.037
$C_7F_{10}H^-$	274.9924	5.938 – 3.262
$C_7F_{11}H_2^-$	294.9986	3.282
$C_7F_9^-$	254.9862	3.265 – 2.682
$C_6F_7^-$	204.9894	1.377
$C_6F_6H^-$	186.9988	5.575
$C_7F_7^-$	216.9894	6.475 – 2.878
$C_7F_6H^-$	198.9988	2.415
$C_7F_5H_2^-$	181.0082	2.262
$C_7F_4H_3^-$	163.0176	2.020

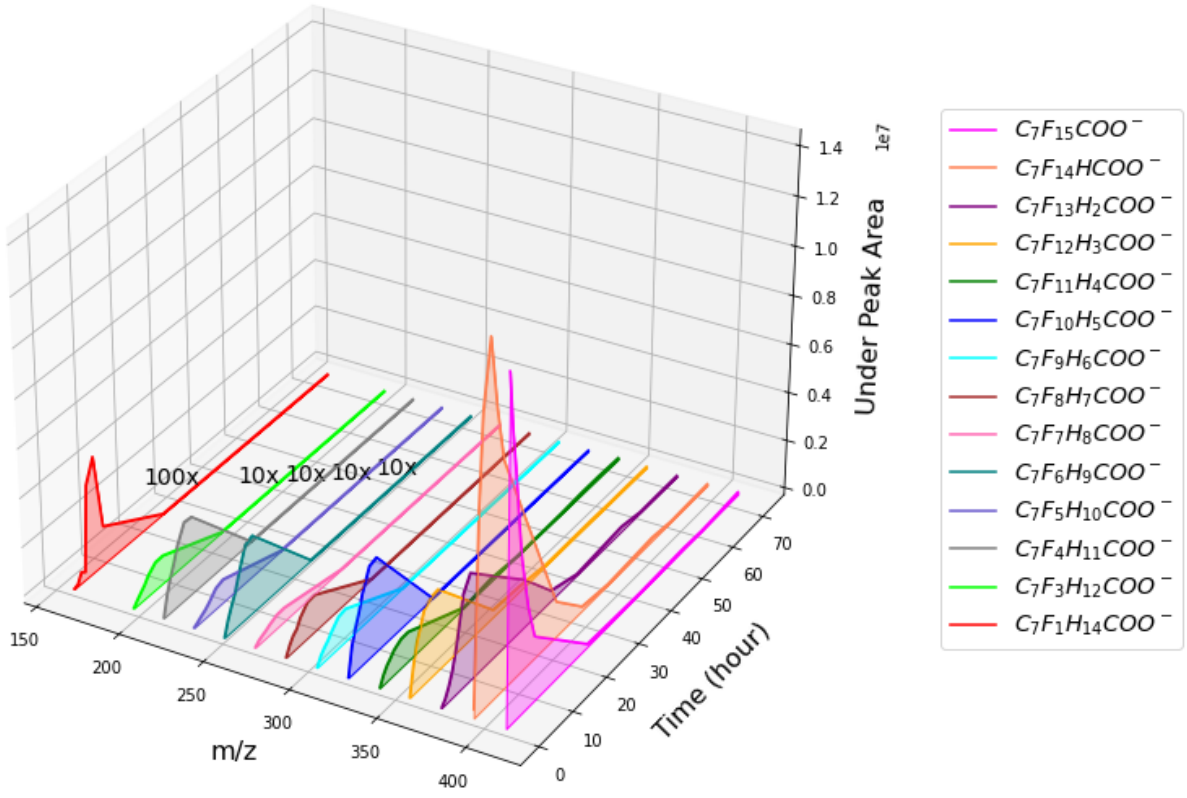

Fig. S19. HR-MS peak areas vs time plot of defluorinated PFAS intermediate products formed during e_{aq}^- mediated defluorination of PFOA with MSN-NH_2-Pd.

Verification of intermediate structures by using MS/MS fragmentation

Collision-induced dissociation (CID) was employed as the fragmentation technique with varying collision energy (CE) spreads (40 ± 20 V) to provide sufficient energy to break bonds with different binding energies (*e.g.* C-H, C-C, C-F, C-O) as well as for the mass dependent CE transfer between the CID gas and the various parent ions. For MS/MS analysis, optimizing CE is crucial for accurate molecule identification, as it governs the energy transferred to ions during fragmentation — where too low CE may result in insufficient fragmentation and too high CE may cause excessive breakdown — both of which can compromise the clarity and abundance of fragment ions necessary for structural identification. In the MS/MS analyses presented here, fragmentation results consistently aligned with the structural identification of partially defluorinated intermediate products. Notably, different isomers exhibited unique fragmentation patterns (**Fig. S19**), highlighting the varying bond stabilities in their structure(s) consistent with our previous observations.

PFOA ($C_7F_{15}COO^-$)

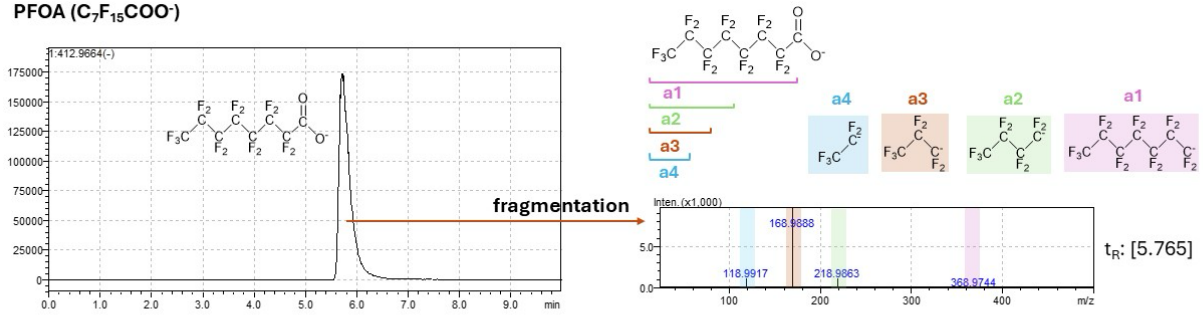

PFOA(1H) ($C_7F_{14}HCOO^-$)

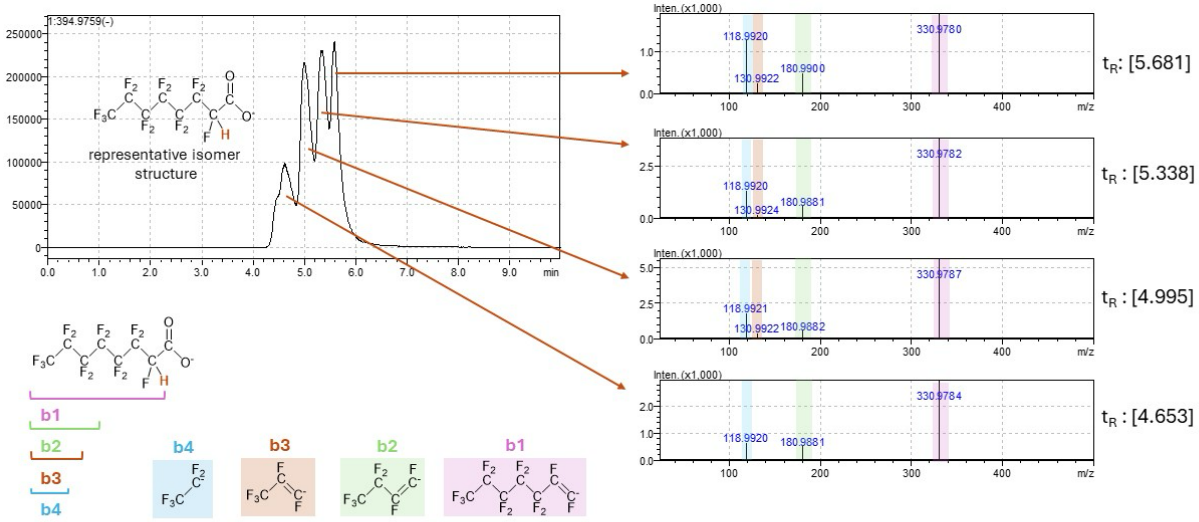

PFOA(2H) ($C_7F_{13}H_2COO^-$)

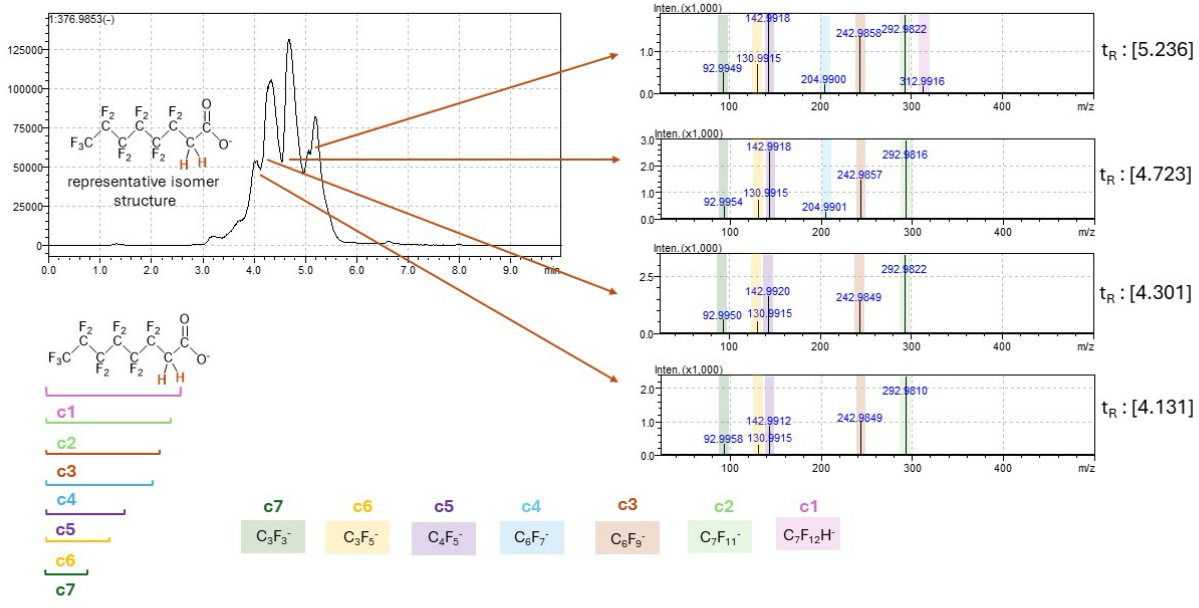

PFOA(3H) ($C_7F_{12}H_3COO^-$)

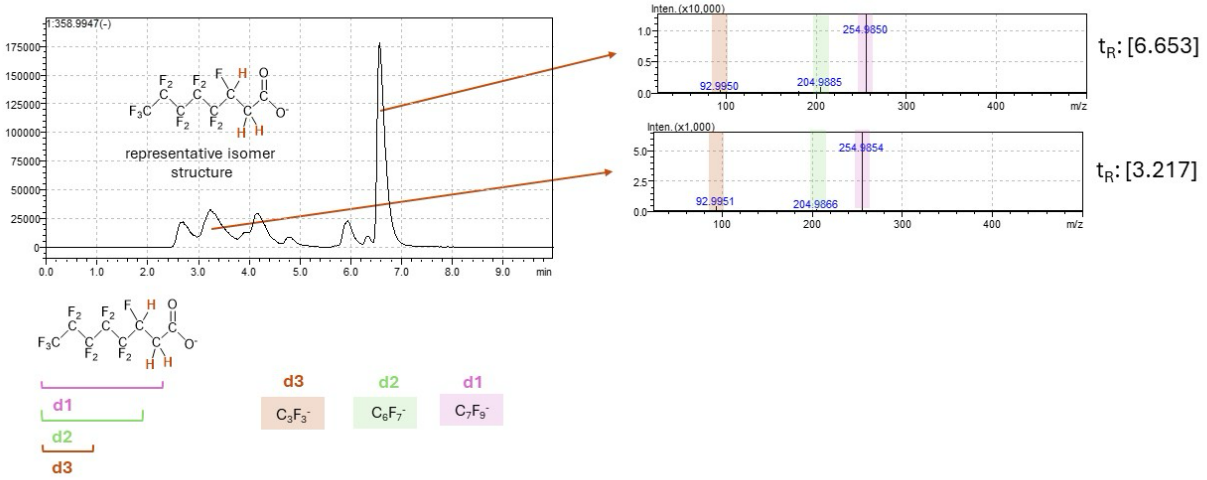

PFOA(4H) ($C_7F_{11}H_4COO^-$)

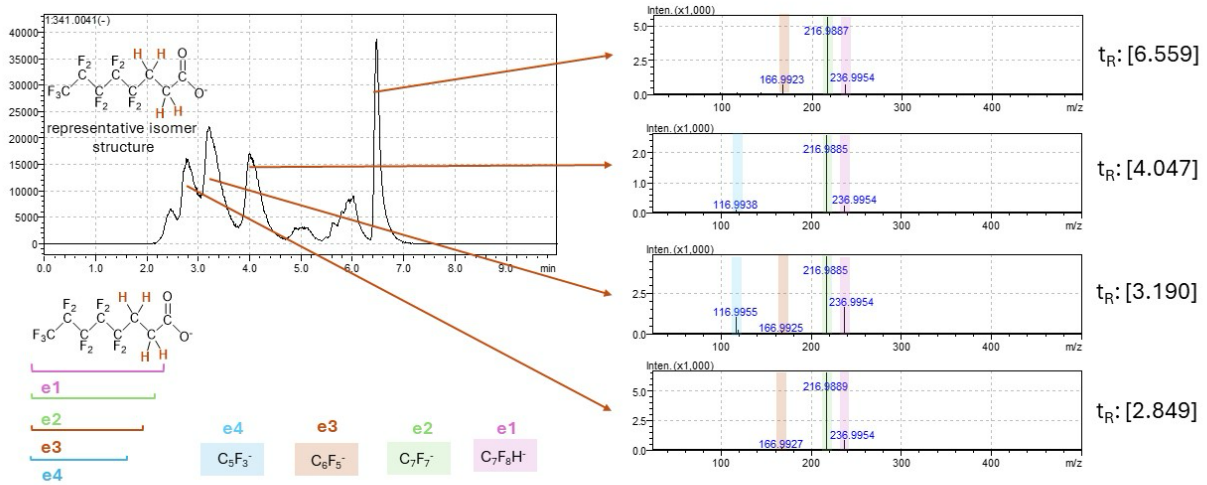

PFOA(5H) ($C_7F_{10}H_5COO^-$)

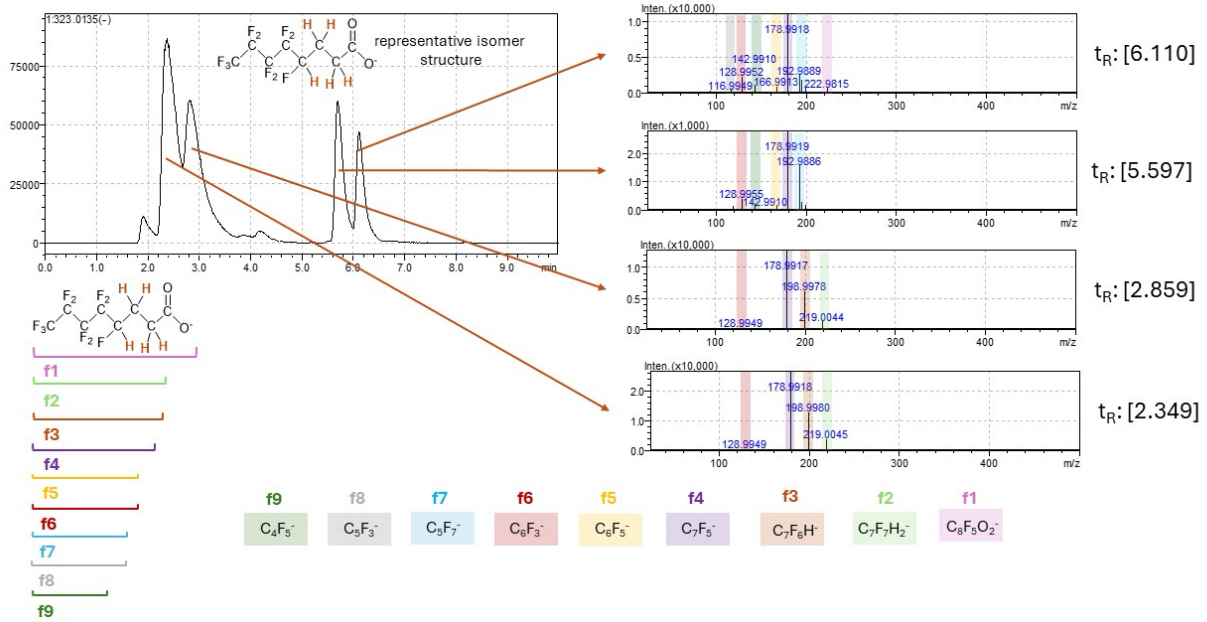

PFOA(6H) ($C_7F_9H_6COO^-$)

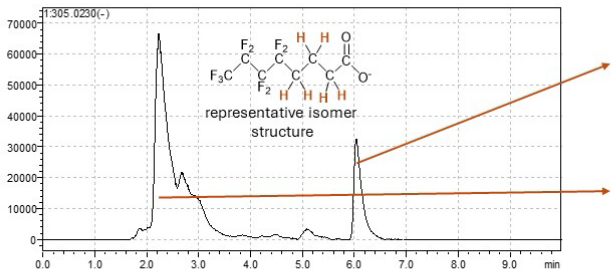

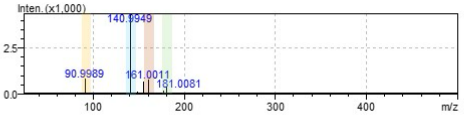

t_R: [6.129]

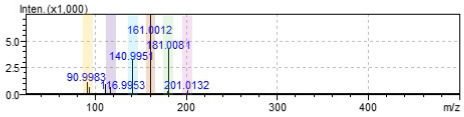

t_R: [2.345]

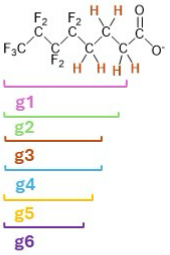

g5	g6	g4	g3	g2	g1
$C_5F_3^-$	C_6F^-	$C_7F_3^-$	$C_7F_4H^-$	$C_7F_5H_2^-$	$C_7F_6H_3^-$

PFOA(7H) ($C_7F_8H_7COO^-$)

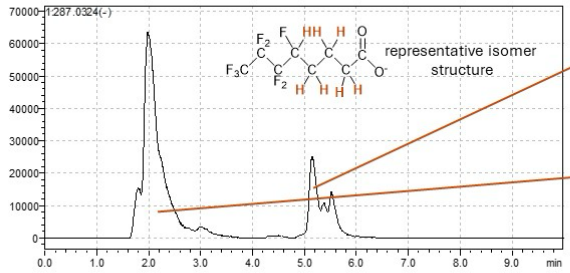

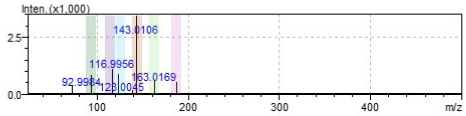

t_R: [5.217]

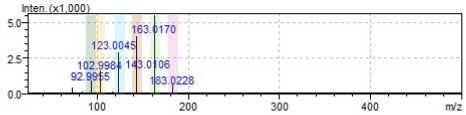

t_R: [2.037]

PFOA(8H) ($C_7F_7H_8COO^-$)

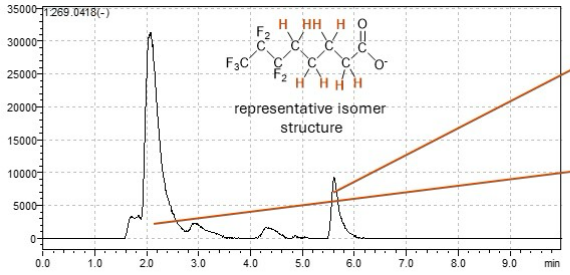

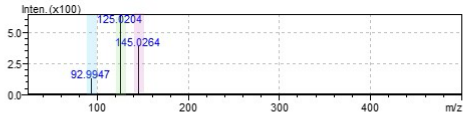

t_R: [5.543]

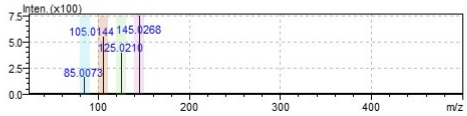

t_R: [2.187]

PFOA(9H) ($C_7F_6H_9COO^-$)

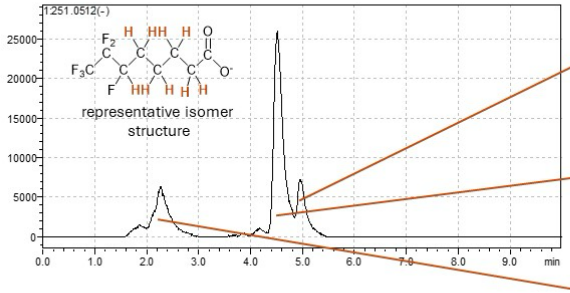

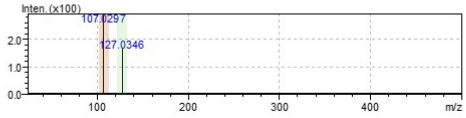

t_R: [5.079]

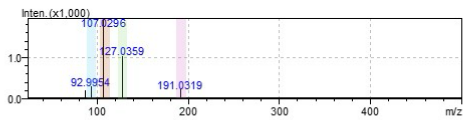

t_R: [4.566]

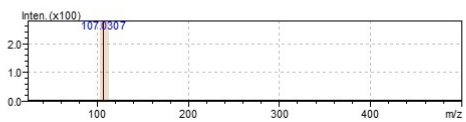

t_R: [2.283]

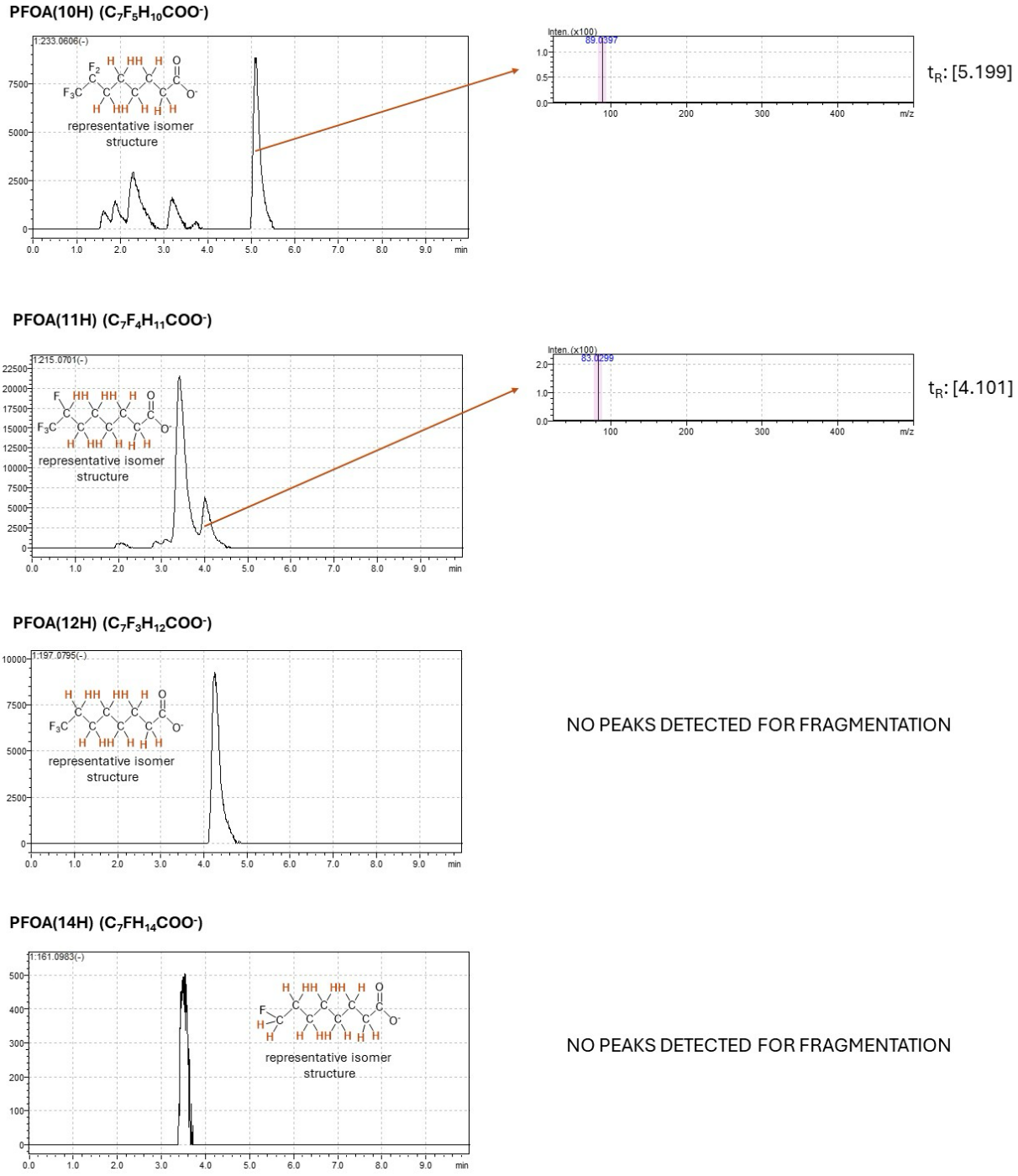

Fig. S20. Not-targeted MS-MS fragmentation analysis of partially defluorinated intermediate products (from PFOA (*m/z* 412.9664) to PFOA(14H) (*m/z* 161.0983)). Please see **Table S6** for associated retention times for each identified species.

Mechanistic discussion for side reactions involved in PFOS degradation

Similar to PFOA degradation, comprehensive LC-HR-MS/MS analysis of PFOS degradation was performed to evaluate reaction pathways. Experimental findings were also compared with previous DFT calculations which evaluate the plausibility of the proposed reaction pathways. Upon attacked by e_{aq}^-, the transformation of PFOS likely involves complex reaction processes such as defluorination, desulfonation, and cleavage of the central C−C bonds[30, 31]. Desulfonatio reaction occurs following the attack of e_{aq}^-, leading to C−S bond breakage. For this process, DFT calculations by others indicate that the bond energy of C−S (272 kJ/mol) in PFOS is lower than that of C−C (346 kJ/mol), facilitating the relatively favorable cleavage of the C−S bond[31]. Additionally, it was reported that the distance between the C and S atoms (4.463 Å) is greater than that of the C−C (1.529–1.627 Å) or S−O (1.651 Å) bonds in PFOS[32]. Further, DFT calculations report that C−S bond stretching occurs upon the association of an extra electron (resulting in the formation of PFOS(1e)), enhancing the probability of head group dissociation[33]. Following desulfonation, the formation and subsequent degradation of PFOA were observed, consistent with findings reported in previous studies[30]. It is important to note that no substantial concentrations of PFOA (or any short-chain PFCAs) were detected during the quantitative LC-MS measurements of PFOS degradation experiments, indicating that the formation of PFOA occurs at relatively trace levels, consistent with the significantly low LC-HR-MS/MS signal intensities. Upon desulfonation, $-CF_2-$ loss was observed during subsequent steps of reductive degradation of the perfluoroalkyl tail formed from PFOS. It has been previously reported that after the attachment of e_{aq}^- to one of the central $-CF_2-$ groups, the adjacent C−C bonds are weakened, thereby facilitating the cleavage of these bonds[31]. Moreover, considering the lowest unoccupied molecular orbitals (LUMOs) of PFOS are located on the C4−C8 atoms within the perfluoroalkyl tail, the formation of smaller perfluoroalkyl chains ($C_7F_{15}^-$, $C_6F_{13}^-$, $C_5F_{11}^-$, etc.) is particularly favorable, as these dissociation fragments of PFOS possess lower relative energies compared to PFOS(1e)[30, 31]. Similarly, a possible cleavage of C−C bonds in PFOS and its partially defluorinated intermediates (PFOS(1H), PFOS(2H), etc.) was observed during the identification of intermediate compounds. Based on substantially lower signal intensities relative to partially defluorinated H/F exchange intermediates, these lower MW species are interpreted as products of parallel side reactions that occur alongside, but do not dominate, the primary (major) defluorination mechanism.

HR-MS chromatogram from 48th hour:

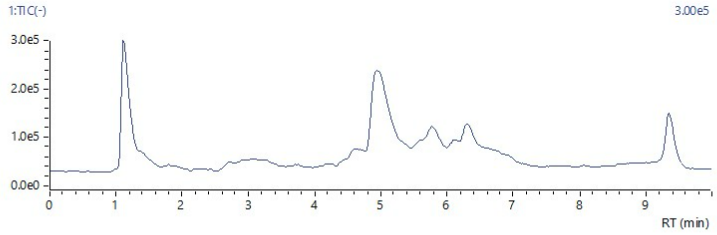

PFOS ($C_8F_{17}SO_3^-$)

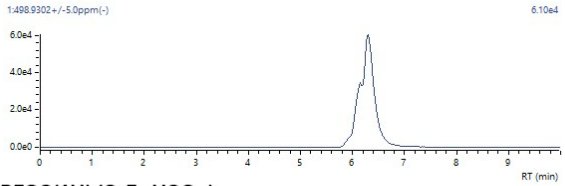

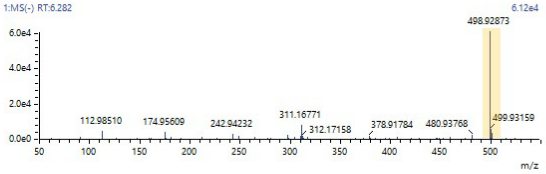

PFOS(1H) ($C_8F_{16}HSO_3^-$)

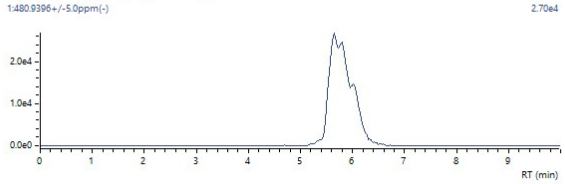

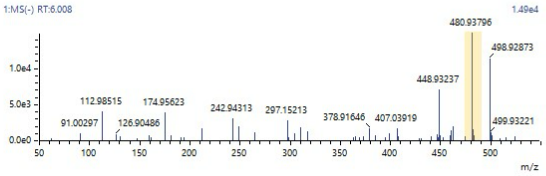

PFOS(2H) ($C_8F_{15}H_2SO_3^-$)

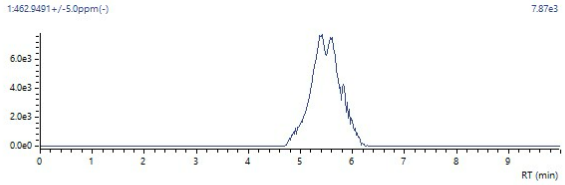

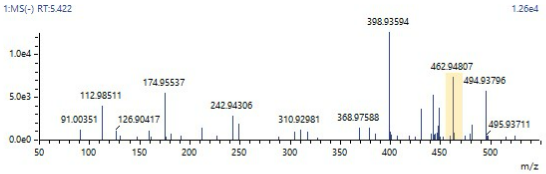

PFOS(3H) ($C_8F_{14}H_3SO_3^-$)

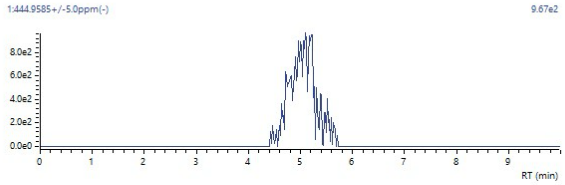

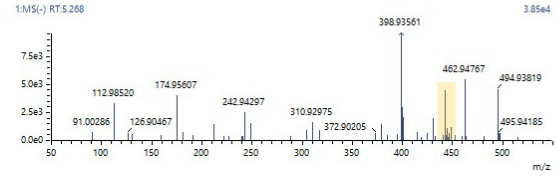

PFOS(17H) ($C_8H_{17}SO_3^-$)

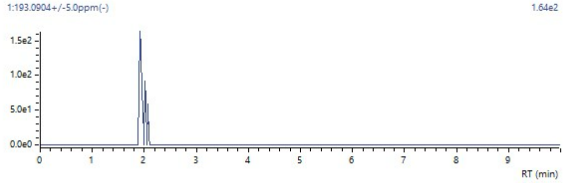

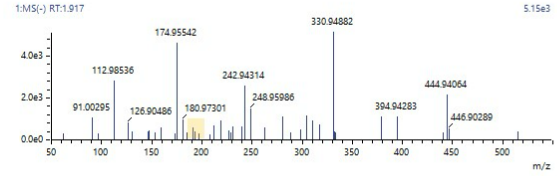

$C_7F_{14}HSO_3^-$

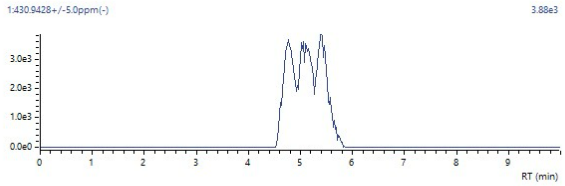

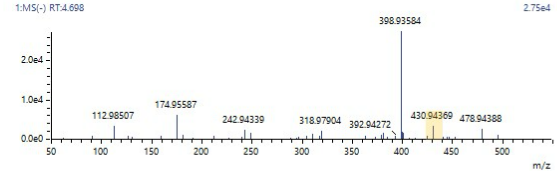

$C_6F_{12}HSO_3^-$

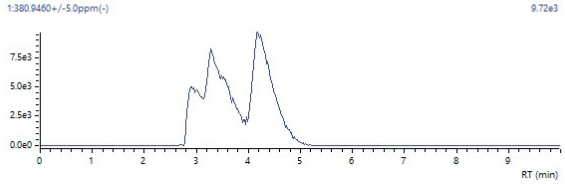

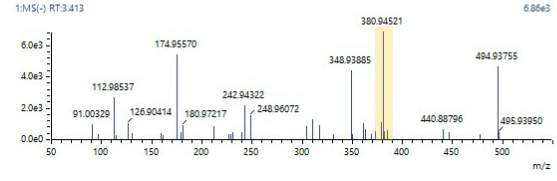

$C_5F_{10}HSO_3^-$

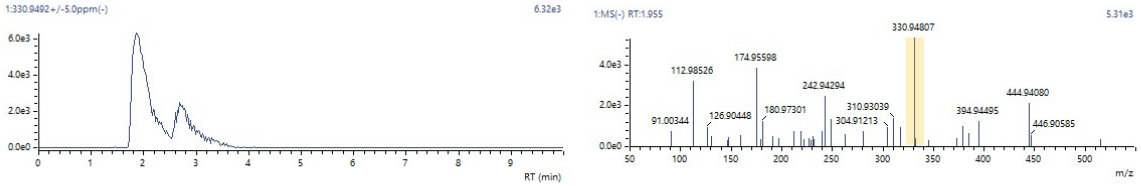

$C_4F_8HSO_3^-$

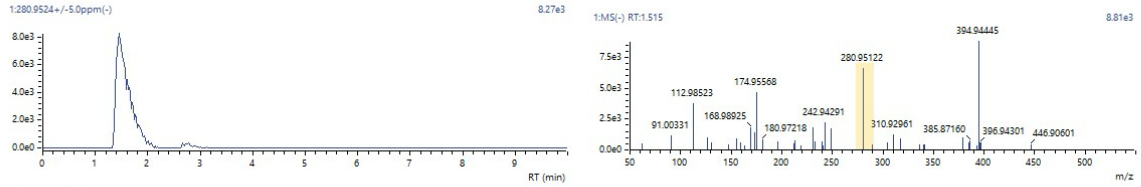

$C_3F_6HSO_3^-$

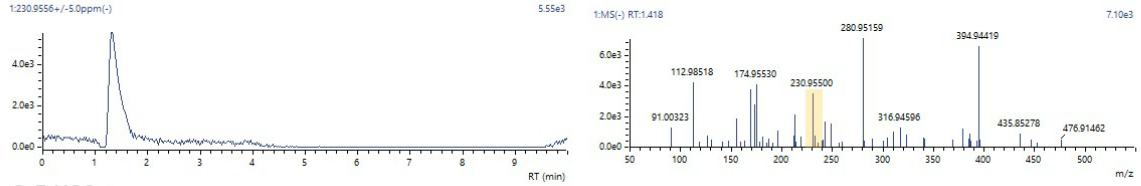

$C_2F_5HSO_3^-$

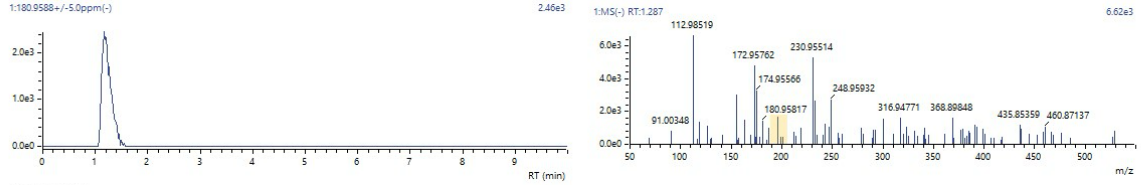

$CF_3HSO_3^-$

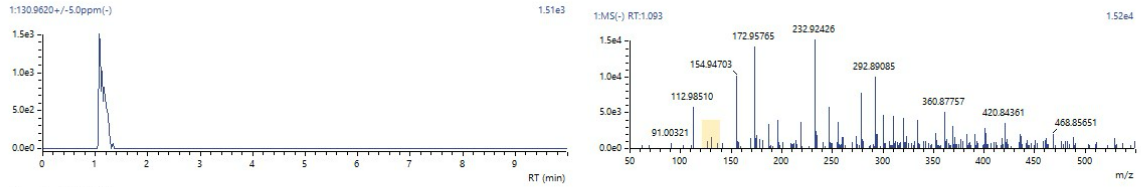

$C_7F_{13}H_2SO_3^-$

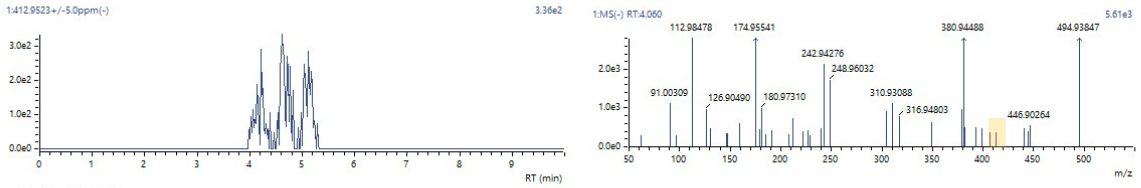

$C_6F_{11}H_2SO_3^-$

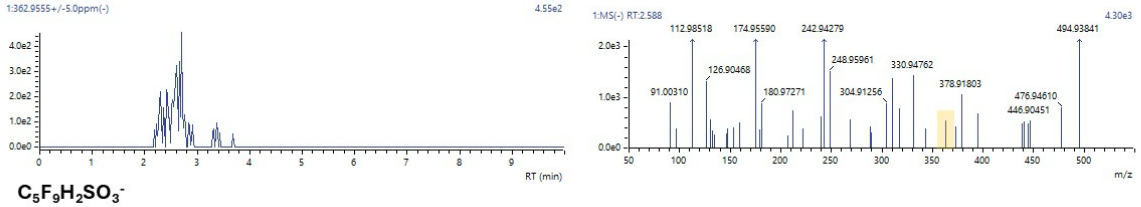

$C_5F_9H_2SO_3^-$

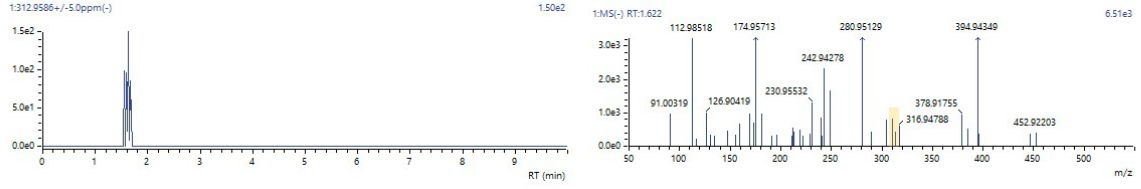

$C_4F_7H_2SO_3^-$

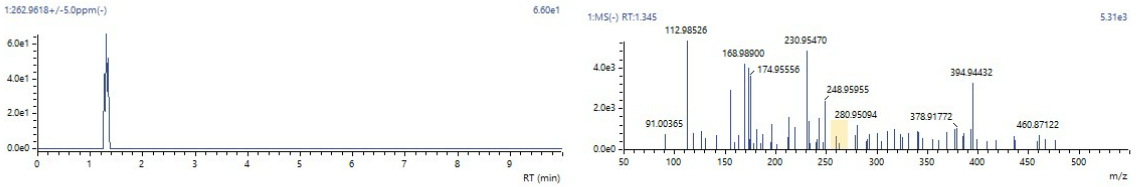

PFOA ($C_7H_{15}COO^-$)

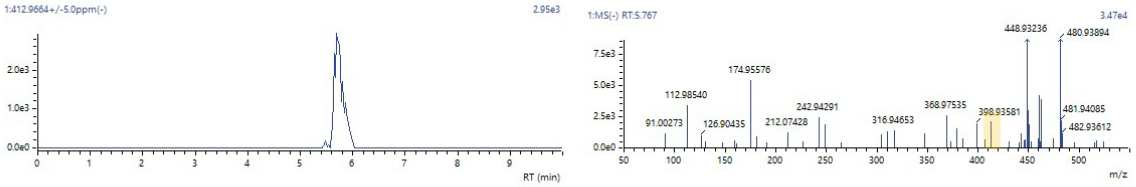

$C_6H_{13}COO^-$

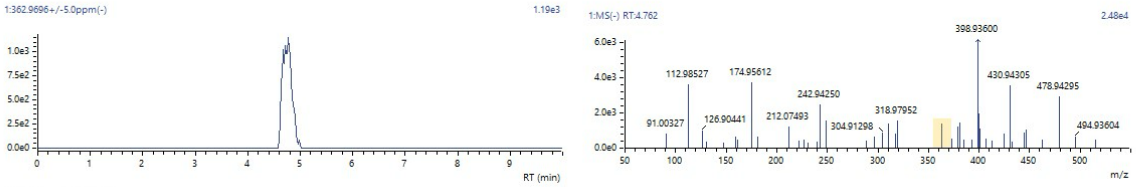

$C_5H_{11}COO^-$

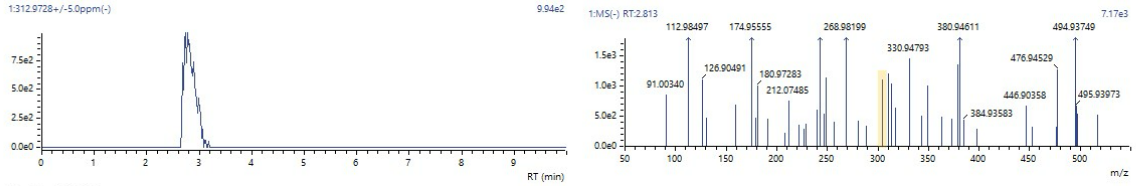

$C_4H_9COO^-$

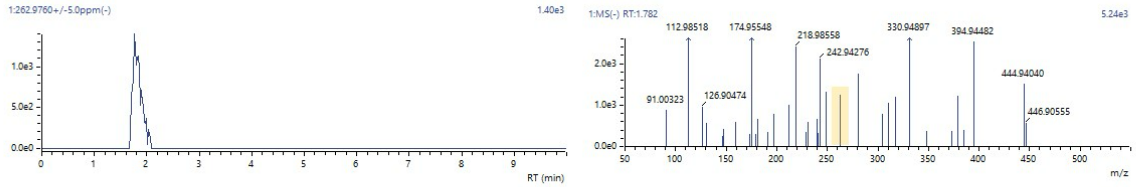

$C_3H_7COO^-$

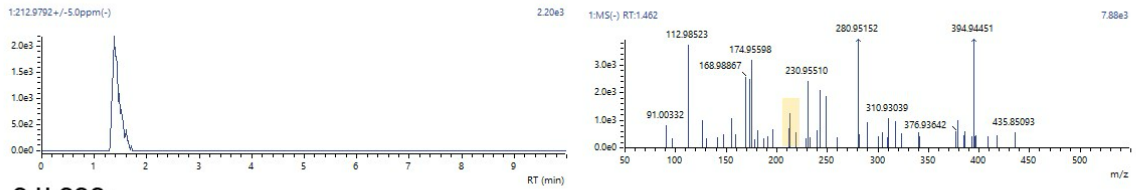

$C_2H_5COO^-$

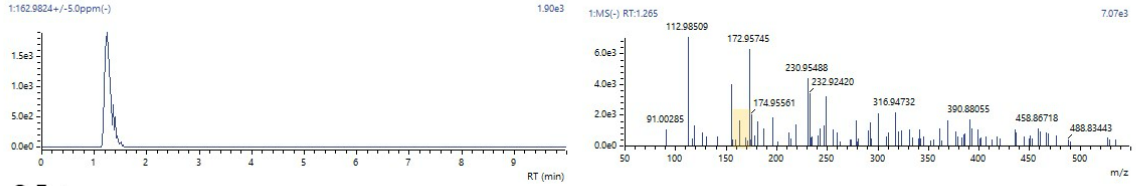

$C_7F_{15}^-$

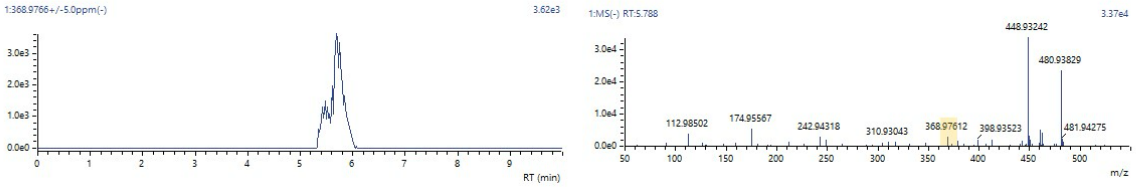

$C_6F_{13}^-$

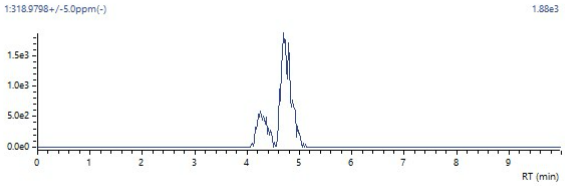

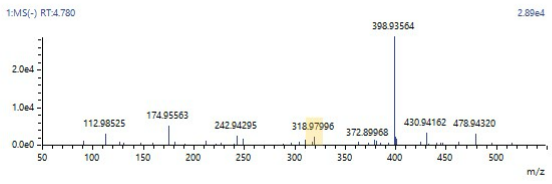

$C_5F_{11}^-$

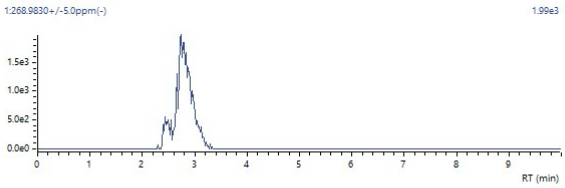

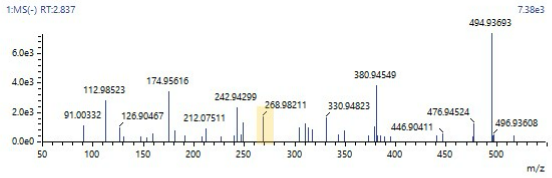

$C_4F_9^-$

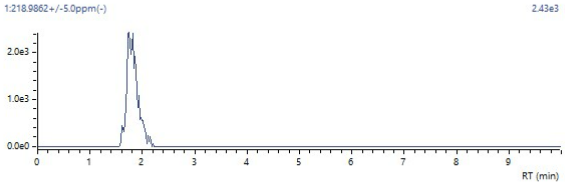

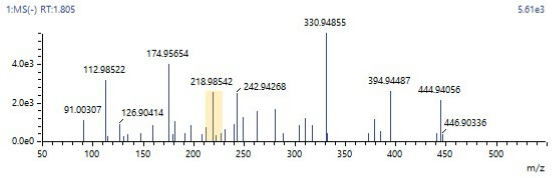

$C_3F_7^-$

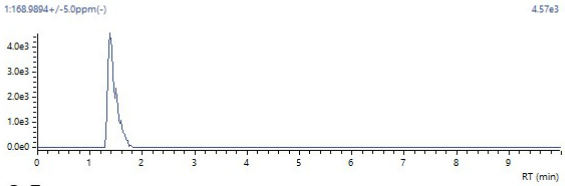

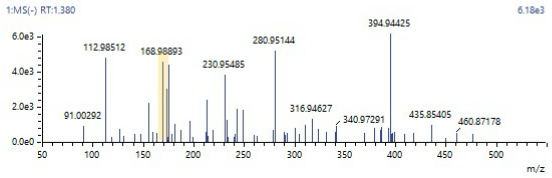

$C_2F_5^-$

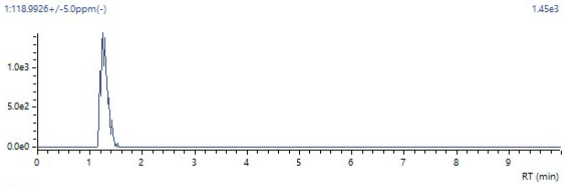

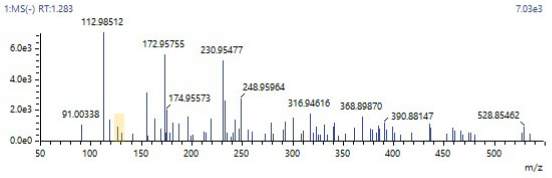

CF_3^-

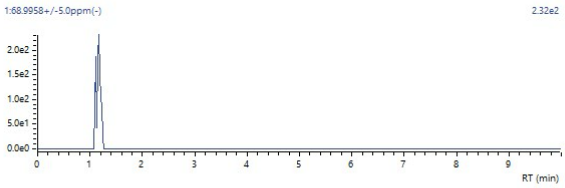

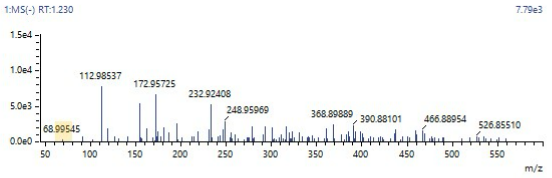

$C_7F_{15}SO_3^-$

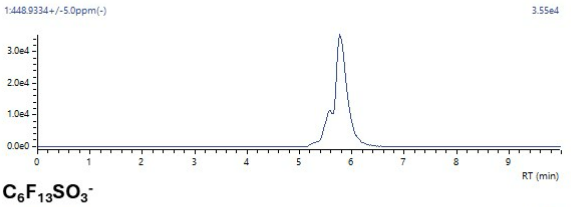

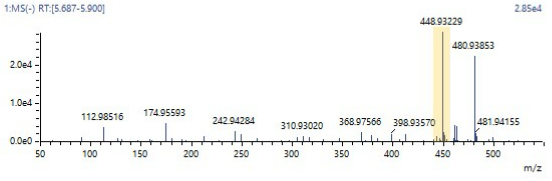

$C_6F_{13}SO_3^-$

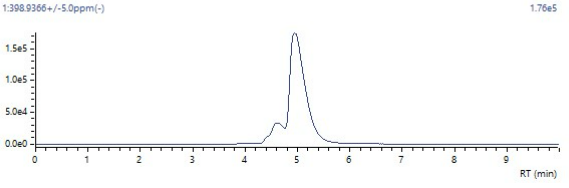

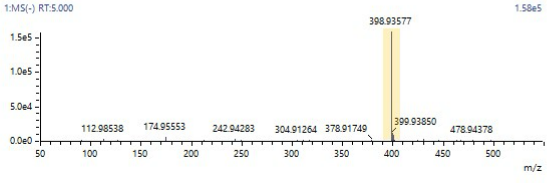

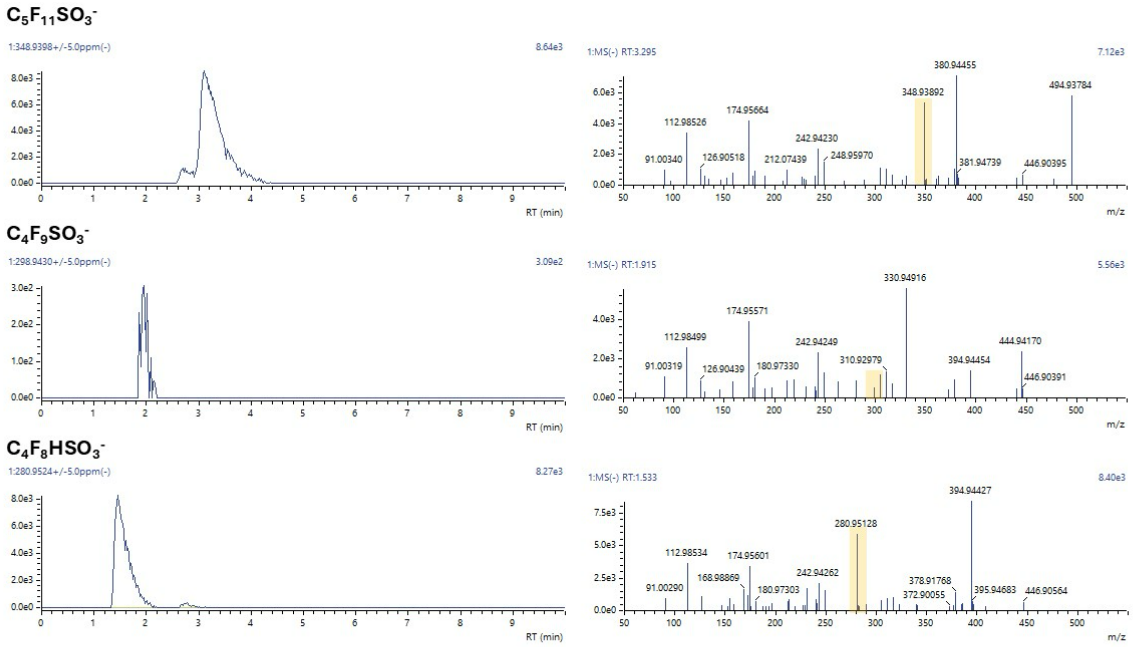

Fig. S21. HR-MS identification of intermediates formed during e_{aq}^- mediated defluorination of PFOS with MSN-NH_2-Pd. Please see **Table S7** for associated retention times for each identified species.

Table S7. Mass-to-charge ratios and retention times of intermediates formed during e_{aq}^- mediated defluorination of PFOS with MSN-NH_2-Pd and identified via HR-MS.

Chemical Formula $[M-H]^-$	Mass-to-charge ratio (*m/z*)	Retention Time (t_R) (min)
$C_8F_{17}SO_3^-$	498.9302	6.361 – 6.190
$C_8F_{16}HSO_3^-$	480.9396	6.015 – 5.844 – 5.672
$C_8F_{15}H_2SO_3^-$	462.9491	5.929 – 5.585 – 5.414
$C_8F_{14}H_3SO_3^-$	444.9585	5.161 – 4.954
$C_8F_{13}H_4SO_3^-$	426.9679	4.924
$C_8H_{17}SO_3^-$	193.0904	1.952
$C_7F_{15}SO_3^-$	448.9334	5.780 – 5.608
$C_6F_{13}SO_3^-$	398.9366	4.921 – 4.615
$C_5F_{11}SO_3^-$	348.9398	3.214 – 2.871
$C_4F_9SO_3^-$	298.9430	4.921 – 4.615
$C_3F_7SO_3^-$	280.9524	2.890 – 1.574
$C_7F_{14}HSO_3^-$	430.9428	5.485 – 5.143 – 4.802
$C_6F_{12}HSO_3^-$	380.9460	4.347 – 3.321 – 2.978
$C_5F_{10}HSO_3^-$	330.9492	2.799 – 1.940
$C_4F_8HSO_3^-$	280.9524	2.890 – 1.574
$C_3F_6HSO_3^-$	230.9556	1.455
$C_2F_4HSO_3^-$	180.9588	1.316
$CF_2HSO_3^-$	130.9620	1.077
$C_7F_{13}H_2SO_3^-$	412.9523	5.098 – 4.889 – 4.092
$C_6F_{11}H_2SO_3^-$	362.9555	3.532 – 2.604 – 2.299
$C_5F_9H_2SO_3^-$	312.9586	1.752
$C_4F_7H_2SO_3^-$	262.9618	1.446
$C_3F_5H_2SO_3^-$	212.9650	1.247
$C_2F_3H_2SO_3^-$	162.9682	1.192
$C_7F_{15}CO_2^-$	412.9664	5.809
$C_6F_{13}CO_2^-$	362.9696	4.857
$C_5F_{11}CO_2^-$	312.9728	2.764
$C_4F_9CO_2^-$	262.9760	1.928
$C_3F_7CO_2^-$	212.9792	1.426
$C_2F_5CO_2^-$	162.9824	1.388
$C_7F_{15}^-$	368.9766	5.754 – 5.582
$C_6F_{13}^-$	318.9798	4.899– 4.356
$C_5F_{11}^-$	268.9830	2.447 – 2.962
$C_4F_9^-$	218.9862	1.882
$C_3F_7^-$	168.9894	1.557
$C_2F_5^-$	118.9926	1.424
CF_3^-	68.9958	1.238

PFOS ($C_8F_{17}SO_3^-$)

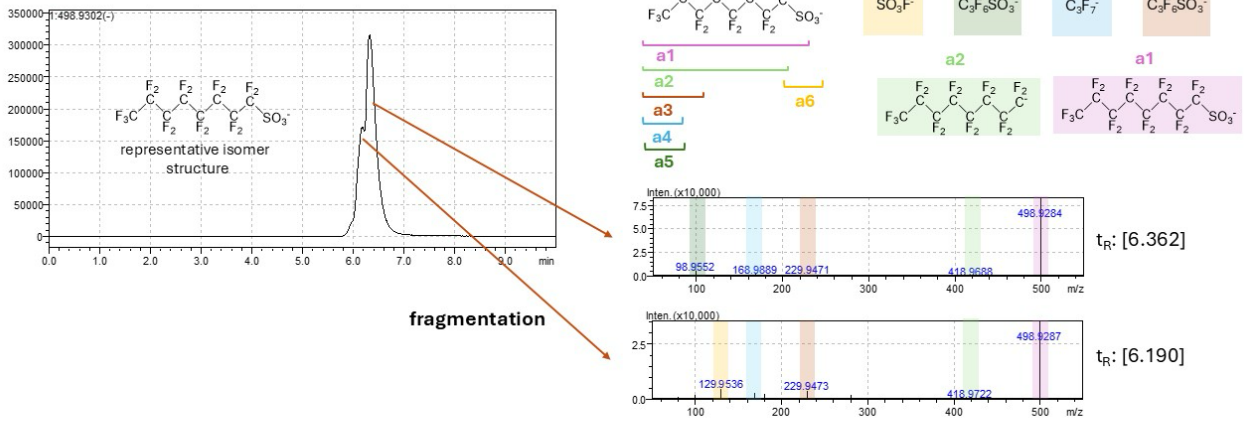

PFOS(1H) ($C_8F_{16}HSO_3^-$)

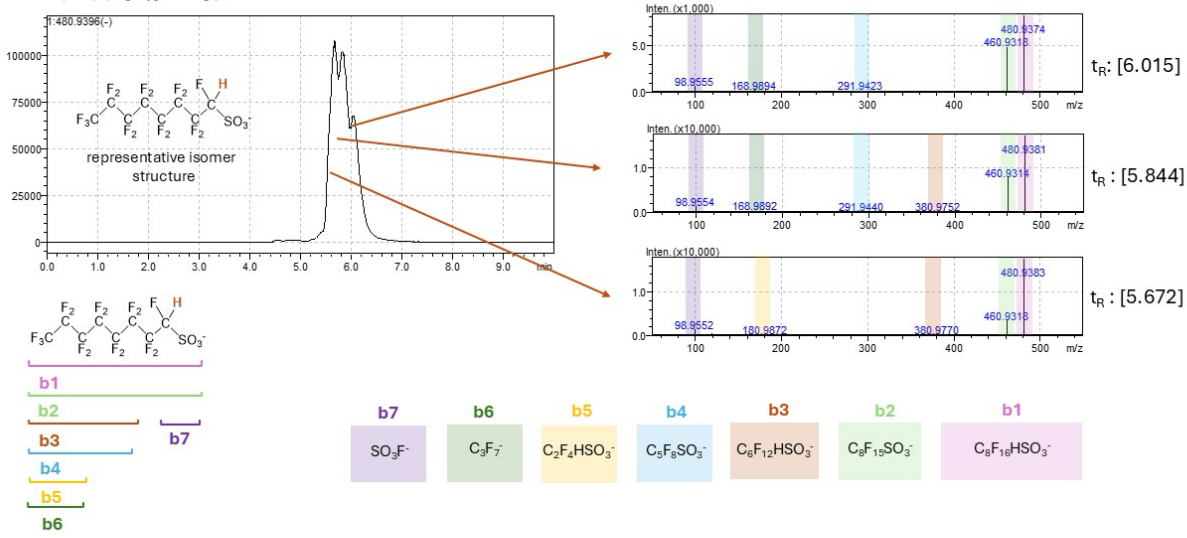

PFOS(2H) ($C_8F_{15}H_2SO_3^-$)

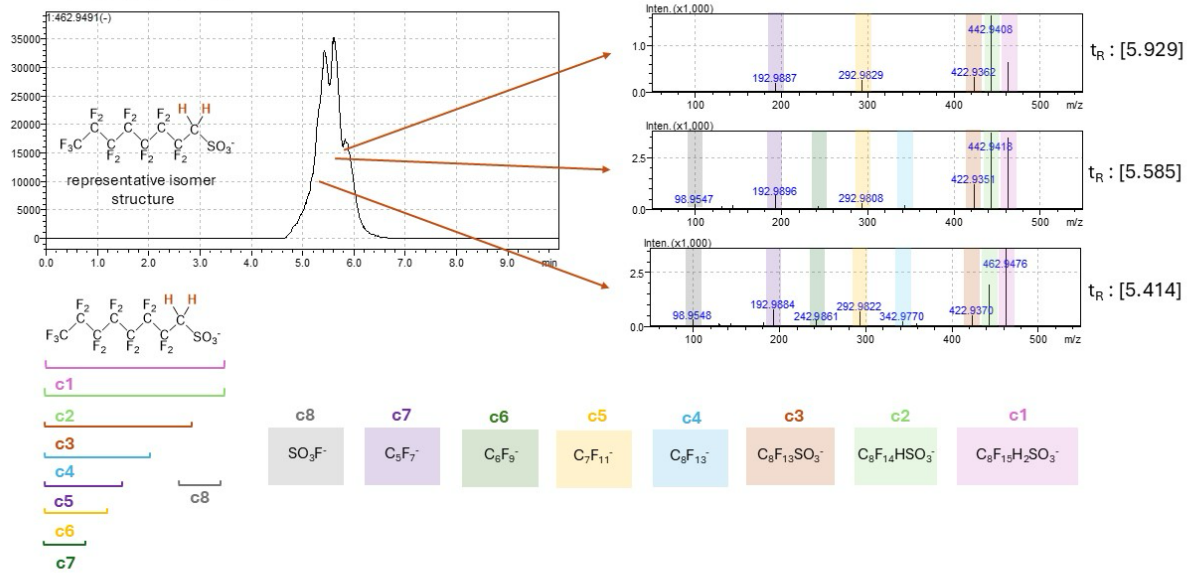

PFOS(3H) ($C_8F_{14}H_3SO_3^-$)

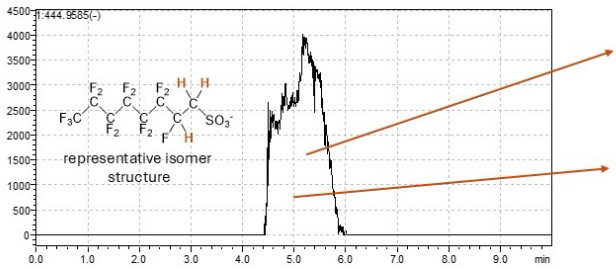

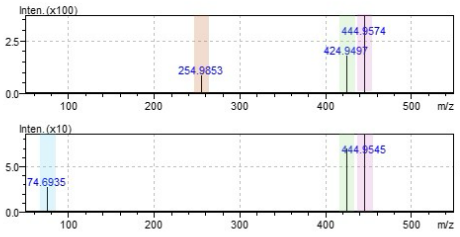

t_R: [5.211-5.161]

t_R: [5.041-4.954]

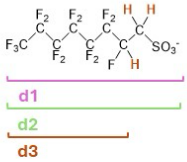

d1

d2

d3

d3	d2	d1
$C_7F_9^-$	$C_8F_{13}H_2SO_3^-$	$C_8F_{14}H_3SO_3^-$

PFOS(4H) ($C_8F_{13}H_4SO_3^-$)

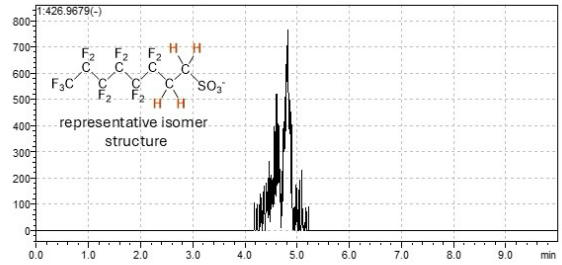

NO PEAKS DETECTED FOR FRAGMENTATION

$C_7F_{14}HSO_3^-$

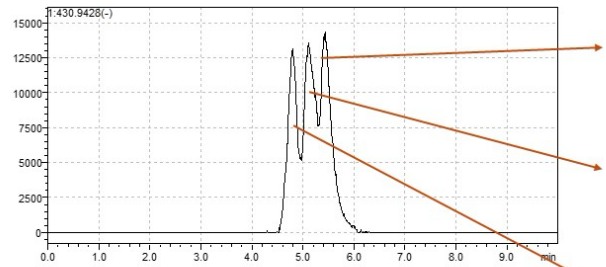

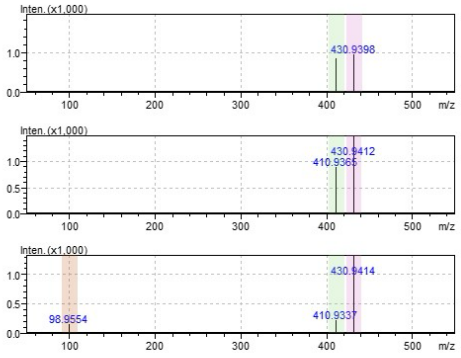

t_R: [5.485]

t_R: [5.143]

t_R: [4.802]

e3	e2	e1
SO_3F^-	$C_7F_{13}SO_3^-$	$C_7F_{14}HSO_3^-$

$C_6F_{12}HSO_3^-$

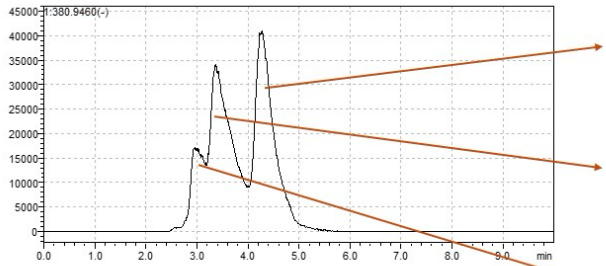

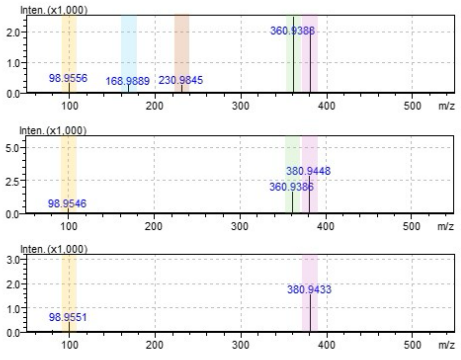

t_R: [4.347]

t_R: [3.321]

t_R: [2.978]

f5	f4	f3	f2	f1
SO_3F^-	$C_3F_7^-$	$C_5F_9^-$	$C_6F_{11}SO_3^-$	$C_6F_{12}HSO_3^-$

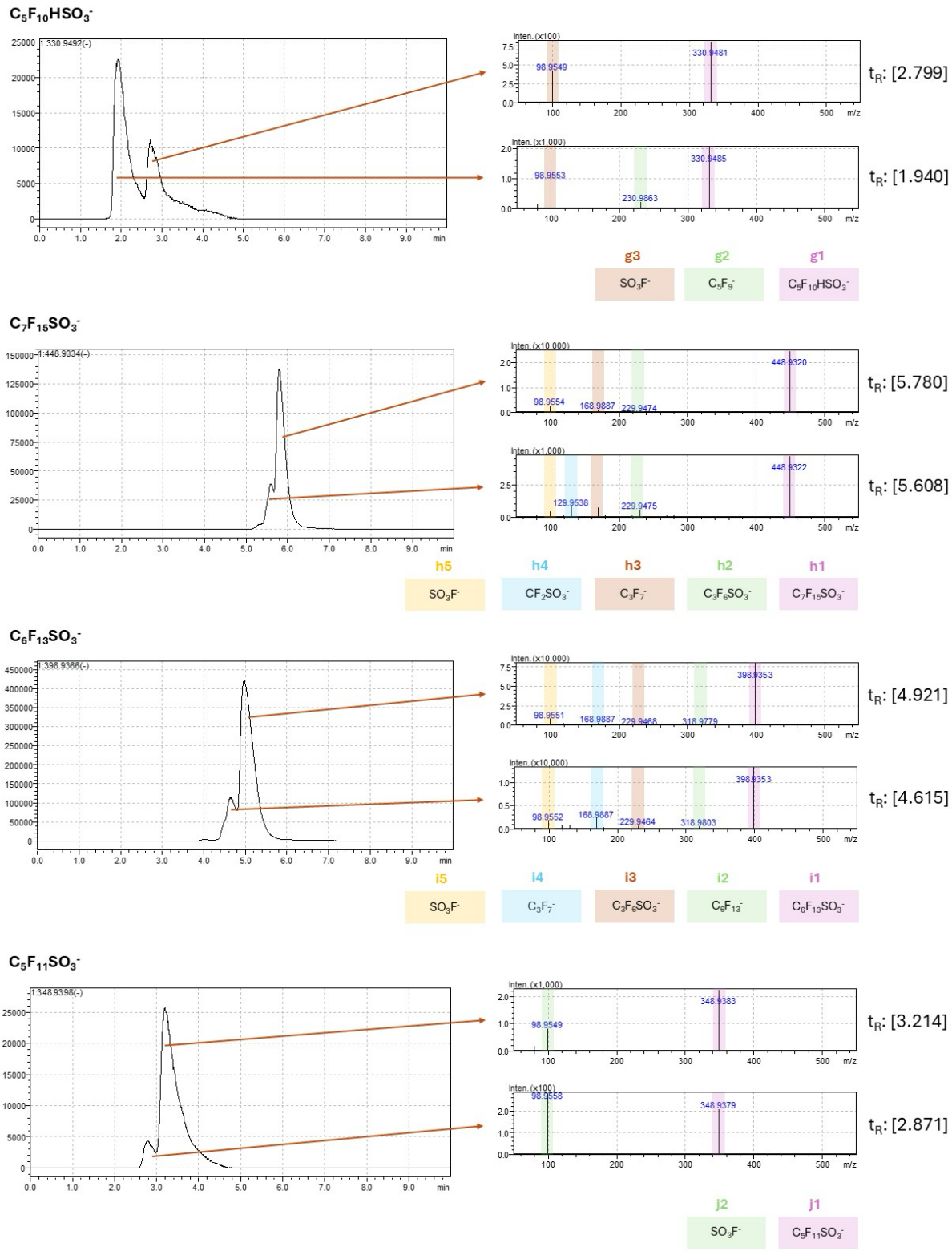

Fig. S22. Not-targeted MS-MS fragmentation analysis of intermediate products of reductive PFOS (*m/z* 498.9302) degradation. Please see **Table S7** for associated retention times for each identified species.

Advanced oxidative processes (AOP)

Conventionally, two (primary) degradation pathways are widely reported in the literature for PFAS degradation: the advanced oxidation pathway (AOP) and the advanced reduction pathway (ARP). AOP can be generally defined as a chain-shortening pathway, which starts with decarboxylation step followed by hydroxylation, elimination, and subsequent hydrolysis of the initial PFAS structure. This process is also known as DHEH (decarboxylation, hydroxylation, elimination, and hydrolysis) and requires the presence of an oxidative species to proceed as illustrated in **Fig. S22**. In this work, the absence (or quenching) of an available oxidative reactant limits the hydroxylation step of DHEH process, thus inhibiting a chain-shortening pathway. Supporting this, we do not observe significant short-chain PFCA compound(s) evolution.

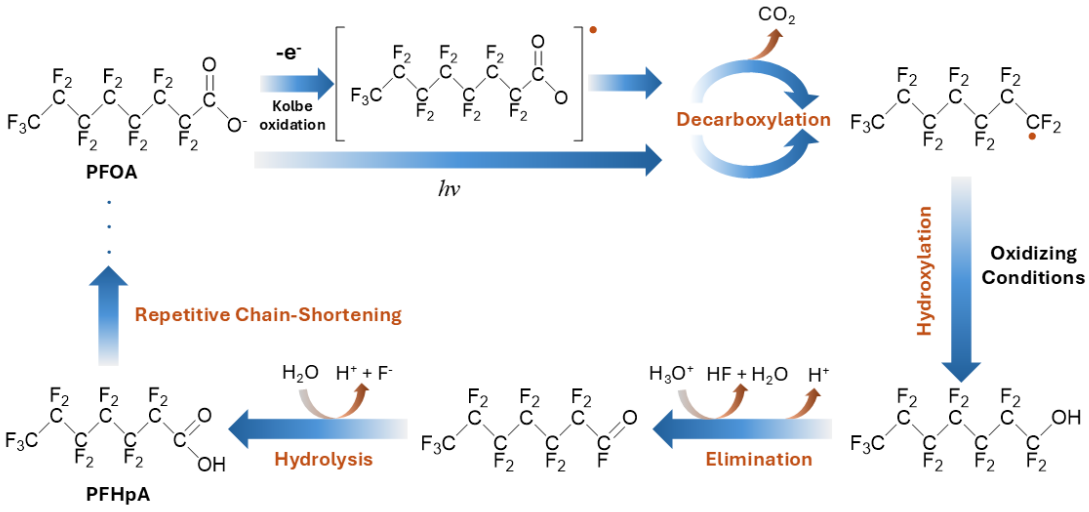

Fig. S23. Oxidative degradation pathway of PFOA through DHEH process.

Approximate Material Cost Calculation for MSN-NH_2-Pd

Approximate material cost calculation for MSN-NH_2-Pd was based on the prices of individual reagents listed by Sigma-Aldrich (USA) as of April 2025. The base material, aminated mesoporous silica nanoparticles (MSN-NH_2), was priced at approximately $1.40 per gram. Using this value as a starting point, the total cost of synthesizing MSN-NH_2-Pd was estimated (**Table S8**) by incorporating the quantity and cost of palladium and platinum precursor used in the deposition step. These preliminary estimates reflect raw material expenses only and do not include operational or labor costs, yet they provide a reasonable basis for evaluating the economic feasibility of the synthesized plasmonic photocatalysts in comparison to commercial alternatives.

Table S8. Breakdown of the approximate material cost calculation for MSN-NH_2-Pd

Step 1.1 – MSN Synthesis			
Chemical	**Amount**	**Cost**	**Unit**
DI H_2O	2600 mL	0.26	$
EtOH (190 proof)	360 mL	0.90	$
CTAB	5.72 g	2.40	$
TEA	11.36 g	0.30	$
TEOS	296 mL	17.5	$
Reaction Parameters			
Reaction Temp.	70 ºC		
Agitation speed	500 rpm		
Reaction time	2 h		
Reaction pH	9.25 @RT		
Reaction vessel	5 L flat-bottom reactor		
Agitator	Overhead stirrer		
Total Cost (before purification)	**76000 mg**	**21.3**	$
Step 1.2 – MSN Purification			
Chemical	**Amount**	**Cost**	**Unit**
EtOH	1400 mL	3.4	$
HCl	20 mL		
Reaction Parameters			
Reaction Temp.	70 ºC		
Agitation speed	500 rpm		
Reaction time	2 h		
Reaction pH	<1		
Reaction vessel	5 L flat-bottom reactor		
Agitator	Overhead stirrer		
Total Yield of MSN		**76000**	mg
Total Cost (after purification)		**24.7**	$
Total Cost (per gram)		**0.33**	$
Step 2 – Amine Functionalization of MSN			
Chemical	**Amount**	**Cost**	**Unit**

APTES	30 mL	15.7	$
MSN	20 g	6.40	$
H_2O	1600 mL	0.16	$
EtOH	2400 mL	5.80	$
Reaction Parameters			
Reaction Temp.	60 ºC		
Agitation speed	500 rpm		
Reaction time	12 h		
Reaction vessel	5 L flat-bottom reactor		
Agitator	Overhead stirrer		
Total yield of MSN-NH_2		**20**	**g**
Total Cost of MSN-NH_2		**27.9**	**$**
Total Cost (per gram)		**1.40**	**$/g**
Step 3 – Pd deposition on MSN-NH_2			
Chemical	**Amount**	**Cost**	**Unit**
MSN-NH_2	8 g	11.2	$
DI H_2O	1000 mL	0.10	$
Sodium citrate, dihydrate	5.42 g	0.08	$
Pd precursor	0.38 g	19.3	$
Reaction Parameters			
Agitation speed	500 rpm		
Reaction Temp.	82 ºC		
Reaction time	20 min		
Reaction vessel	2.5 L flat-bottom beaker		
Agitator	Overhead stirrer		
Inert gas	N_2		
Total cost of MSN-NH_2-Pd		**30.5**	$
Total Yield of MSN-NH_2-Pd		**8**	**g**
Unit cost of MSN-NH_2-Pd		**3.8**	**$/g**

References

1. Moller, K., Kobler, J. & Bein, T. Colloidal suspensions of nanometer-sized mesoporous silica. *Adv Funct Mater* **17**, 605-612 (2007).
2. Xu, S., Hartvickson, S. & Zhao, J.X. Increasing Surface Area of Silica Nanoparticles With a Rough Surface. *ACS Applied Materials & Interfaces* **3**, 1865-1872 (2011).
3. Buxton, G.V., Greenstock, C.L., Helman, W.P. & Ross, A.B. Critical Review of rate constants for reactions of hydrated electrons, hydrogen atoms and hydroxyl radicals (·OH/·O− in Aqueous Solution. *Journal of Physical and Chemical Reference Data* **17**, 513-886 (1988).
4. Zelko, I.N., Mariani Tj Fau - Folz, R.J. & Folz, R.J. Superoxide dismutase multigene family: a comparison of the CuZn-SOD (SOD1), Mn-SOD (SOD2), and EC-SOD (SOD3) gene structures, evolution, and expression.
5. Vel Leitner, N.K., Guilbault, I. & Legube, B. Reactivity of OH and e−aq from electron beam irradiation of aqueous solutions of EDTA and aminopolycarboxylic acids. *Radiation Physics and Chemistry* **67**, 41-49 (2003).
6. Wen, Y. et al. Integrated Photocatalytic Reduction and Oxidation of Perfluorooctanoic Acid by Metal–Organic Frameworks: Key Insights into the Degradation Mechanisms. *Journal of the American Chemical Society* **144**, 11840-11850 (2022).
7. Camdzic, D. et al. Quantitation of Total PFAS Including Trifluoroacetic Acid with Fluorine Nuclear Magnetic Resonance Spectroscopy. *Analytical Chemistry* **95**, 5484-5488 (2023).
8. Bhat, A.P. et al. Tracking Fluorine during Aqueous Photolysis and Advanced UV Treatment of Fluorinated Phenols and Pharmaceuticals Using a Combined 19F-NMR, Chromatography, and Mass Spectrometry Approach. *ACS Environmental Au* **2**, 242-252 (2022).
9. Gerken, J.B. Measurement of pH by NMR spectroscopy in concentrated aqueous fluoride buffers. *Journal of Fluorine Chemistry* **132**, 68-70 (2011).
10. Heerah, K., Waclawek, S., Konzuk, J. & Longstaffe, J.G. Benchtop 19F NMR spectroscopy as a practical tool for testing of remedial technologies for the degradation of perfluorooctanoic acid, a persistent organic pollutant. *Magnetic Resonance in Chemistry* **58**, 1160-1167 (2020).
11. Lewis, R.E., Huang, C.-H., White, J.C. & Haynes, C.L. Using 19F NMR to Investigate Cationic Carbon Dot Association with Per- and Polyfluoroalkyl Substances (PFAS). *ACS Nanoscience Au* **3**, 408-417 (2023).
12. Camdzic, D., Dickman, R.A. & Aga, D.S. Total and class-specific analysis of per- and polyfluoroalkyl substances in environmental samples using nuclear magnetic resonance spectroscopy. *Journal of Hazardous Materials Letters* **2**, 100023 (2021).
13. C.H. Dungan, J.R.V.W. Compilation of Reported F19 NMR Chemical Shifts. (Wiley Interscience, New York; 1970).
14. Alam, M.S., Rao, B.S.M. & Janata, E. OH reactions with aliphatic alcohols: evaluation of kinetics by direct optical absorption measurement. A pulse radiolysis study. *Radiation Physics and Chemistry* **67**, 723-728 (2003).
15. Long, M. et al. Adsorption and Reductive Defluorination of Perfluorooctanoic Acid over Palladium Nanoparticles. *Environmental Science & Technology* **55**, 14836-14843 (2021).
16. Li, M., Rasamani, K.D. & Sun, Y. Highly Dispersed Palladium Nanoparticles on Silica Spheres for Photocatalytic Hydrodeoxygenation of Vanillin. *The Journal of Physical Chemistry C* **125**, 16550-16556 (2021).
17. Luna, A.L. et al. Photocatalytic Hydrogen Evolution Using Ni–Pd/TiO2: Correlation of Light Absorption, Charge-Carrier Dynamics, and Quantum Efficiency. *The Journal of Physical Chemistry C* **121**, 14302-14311 (2017).
18. Hang Li, Y. et al. Unidirectional suppression of hydrogen oxidation on oxidized platinum clusters. *Nature Communications* **4**, 2500 (2013).

19. Yamijala, S.S.R.K.C., Shinde, R. & Wong, B.M. Real-time degradation dynamics of hydrated per- and polyfluoroalkyl substances (PFASs) in the presence of excess electrons. *Physical Chemistry Chemical Physics* **22**, 6804-6808 (2020).
20. Liu, J. et al. Reductive Defluorination of Branched Per- and Polyfluoroalkyl Substances with Cobalt Complex Catalysts. *Environmental Science & Technology Letters* **5**, 289-294 (2018).
21. Su, Y. et al. Potential-Driven Electron Transfer Lowers the Dissociation Energy of the C–F Bond and Facilitates Reductive Defluorination of Perfluorooctane Sulfonate (PFOS). *ACS Applied Materials & Interfaces* **11**, 33913-33922 (2019).
22. Xiao, F. et al. Thermal Stability and Decomposition of Perfluoroalkyl Substances on Spent Granular Activated Carbon. *Environmental Science & Technology Letters* **7**, 343-350 (2020).
23. Alinezhad, A. et al. Mechanistic Investigations of Thermal Decomposition of Perfluoroalkyl Ether Carboxylic Acids and Short-Chain Perfluoroalkyl Carboxylic Acids. *Environmental Science & Technology* **57**, 8796-8807 (2023).
24. Longendyke, G.K., Katel, S. & Wang, Y. PFAS fate and destruction mechanisms during thermal treatment: a comprehensive review. *Environmental Science: Processes & Impacts* **24**, 196-208 (2022).
25. Zhou, L., Huang, Q. & Xia, Y. Plasmon-Induced Hot Electrons in Nanostructured Materials: Generation, Collection, and Application to Photochemistry. *Chem Rev* **124**, 8597-8619 (2024).
26. Anzabi, L.C. et al. Nanoscale 3D spatial analysis of FTO/ZnO/Ag-x films subjected to photocatalytic activity. *Scientific Reports* **15**, 7330 (2025).
27. Huh, H., Trinh, H.D., Lee, D. & Yoon, S. How Does a Plasmon-Induced Hot Charge Carrier Break a C–C Bond? *ACS Applied Materials & Interfaces* **11**, 24715-24724 (2019).
28. Mateo, D., Cerrillo, J.L., Durini, S. & Gascon, J. Fundamentals and applications of photo-thermal catalysis. *Chemical Society Reviews* **50**, 2173-2210 (2021).
29. Cheng, P. et al. Probing SPR heating of metal nanostructures coated on fiber based plasmonic sensor. *Chemical Physics Letters* **738**, 136869 (2020).
30. Cui, J., Gao, P. & Deng, Y. Destruction of Per- and Polyfluoroalkyl Substances (PFAS) with Advanced Reduction Processes (ARPs): A Critical Review. *Environmental Science & Technology* **54**, 3752-3766 (2020).
31. Gu, Y., Dong, W., Luo, C. & Liu, T. Efficient Reductive Decomposition of Perfluorooctanesulfonate in a High Photon Flux UV/Sulfite System. *Environmental Science & Technology* **50**, 10554-10561 (2016).
32. Erkoç, Ş. & Erkoç, F. Structural and electronic properties of PFOS and LiPFOS. *Journal of Molecular Structure: THEOCHEM* **549**, 289-293 (2001).
33. Bentel, M.J. et al. Defluorination of Per- and Polyfluoroalkyl Substances (PFASs) with Hydrated Electrons: Structural Dependence and Implications to PFAS Remediation and Management. *Environmental Science & Technology* **53**, 3718-3728 (2019).